



Article

Analysis of Ni-Cu Interaction in Aluminum-Based Alloys: Hardness, Tensile and Precipitation Behavior

Ehab Samuel ¹, Agnes M. Samuel ¹, Victor Songmene ² , Herbert W. Doty ³ and Fawzy H. Samuel ^{1,*} 

¹ Département des Sciences Appliquées, Université du Québec à Chicoutimi, Saguenay, QC G7H 2B1, Canada; ehafbhsamuel@gmail.com (E.S.); agnesmsamuel@gmail.com (A.M.S.)

² Département de Génie Mécanique, École de Technologie Supérieure, Montreal, QC H3C 1K3, Canada; victor.songmene@etsmtl.ca

³ Materials Technology, General Motors Global Technology Center, Warren, MI 48092, USA; herb.doty@gm.com

* Correspondence: fawzy-hosny.samuel@etsmtl.ca

Abstract: The present work was aimed at quantifying the effects of Ni addition in the range of 0–4% together with 0.3%Zr on the hardness and the tensile properties, volume fraction of intermetallics, and changes in size and distribution of phase precipitation in Sr-modified Al-9%Si-2%Cu-0.6%Mg cast alloys. The study was mainly carried out using high-resolution FESEM and TEM microscopes equipped with EDS facilities. Samples were solidified at the rate of ~ 3 °C/s and examined at different aging conditions. The investigations are supported by thermal analysis carried out at a solidification rate of ~ 0.8 °C/s. The results revealed that the main compositions of the Ni-based phases are close to Al₃(Ni,Cu), Al₃CuNi, and Al₃Ni. An Al₃Ni₂Cu₂ phase was also detected in the 4%Ni alloy. The Cu–Ni phases were observed to precipitate, covering the surfaces of pre-existing primary Al₃Zr particles. The TEM analysis indicated the magnitude of the reduction in both size and density of the precipitated Al₂Cu phase particles as the Ni content reached 4%, coupled with a delay in the transition from coherent to incoherency of the Al₂Cu precipitates.

Keywords: Al–Si alloys; Ni; Zr; HR-TEM; FESEM



Citation: Samuel, E.; Samuel, A.M.; Songmene, V.; Doty, H.W.; Samuel, F.H. Analysis of Ni-Cu Interaction in Aluminum-Based Alloys: Hardness, Tensile and Precipitation Behavior. *Materials* **2024**, *17*, 4676. <https://doi.org/10.3390/ma17184676>

Academic Editor: Jordi Sort

Received: 23 July 2024

Revised: 29 August 2024

Accepted: 30 August 2024

Published: 23 September 2024



Copyright: © 2024 by the authors. Licensee MDPI, Basel, Switzerland. This article is an open access article distributed under the terms and conditions of the Creative Commons Attribution (CC BY) license (<https://creativecommons.org/licenses/by/4.0/>).

1. Introduction

In general, the mechanism of alloy hardening by precipitation results in the formation of coherent clusters of solute atoms; that is, the solute atoms gathered in a cluster must always have the same crystal structure as the phase of the solvent. This then creates a lot of distortion because the crystal parameters of the precipitates can be slightly different from those of the metal matrix [1–9]. The Guinier–Preston or GP zones (solute clusters) and coherent precipitates are effective in blocking dislocations from moving, given the significant stress and strain fields that surround them. The dislocations, to pass the coherent precipitates, have no choice and must shear them, hence increasing the stress required to deform the part [10–19].

Addition of copper (Cu) to aluminum-based alloys would lead to precipitation of Al₂Cu phase particles during the solidification process. Dissolution of Al₂Cu fine particles during solutionizing treatment may occur in 2 h at 495 °C solutionizing temperature. Which is not the case for massive Al₂Cu particles where segregation may take place, leading to incipient melting and hence poor mechanical properties. The combined addition of Cu and Mg will result in balancing the alloy mechanical strength through the mutual precipitation of Al₂Cu and Mg₂Si phase particles [20–24].

Zirconium (Zr) may be used in Al alloys to refine the grain structure due to the precipitation of fine coherent dispersoids (i.e., Al₃Zr), which obstruct dislocation motion, leading to enhancement of the high temperature mechanical properties of aluminum alloys [25]. In order to increase the volume fraction of Al₃Zr precipitates, and based on the phase diagram of Al–Zr, the concentration of Zr in the alloys investigated in this study

was kept at around 0.3 wt% [26]. According to Nakamura et al. [27], the addition of Ag to Al-based alloys containing Mg reduces the size of the precipitates and promotes the precipitation of numerous fine-scale AlMgAg particles, leading to improvement of the alloy mechanical properties.

Nickel (Ni) has a relatively lower contribution to the alloy mechanical performance of aluminum–silicon (Al–Si)-based alloys compared to that produced by the addition of copper (Cu) and magnesium (Mg). Nickel has traditionally been used in a proportion of 2–3% because it was believed to improve the mechanical properties of alloys used at high temperatures [26–29]. The nickel compounds dispersed inside the microstructure suggest that the mechanical properties are improved by the presence of nickel [30–33]. However, the inter-particle spacing of Al₃Ni compounds being considerable, of the order of 50 μm, this large distance would not allow perceptible dispersion hardening. Furthermore, it could be possible that the nickel compounds are formed via a fiber hardening process, but this would not make a significant contribution since the network of silicon fibers in large volume would annihilate this effect of nickel [34–37].

The use of Ni is limited to alloys used in atomic reactors due to its high neutron absorption, but in other applications, its addition is desirable: combined with Fe, for example, it improves resistance to high vapor pressure corrosion [38]. It was reported that the addition of Cu (1.0 to 1.8%) and Ni (1.0 to 1.6%), or just Cu, to eutectic Al–Si alloys produces multicomponent phases of the following types: Al₄₀Si₇(Fe,Mn)₁₁Cu, Al₄₀Si₄Fe₂MnCuNi₁₁, and Al₄₀Si(Fe,Mn,Cu,Ni)₁₃ [39–42].

This present study is in continuity with the previous work carried out by the current authors [43–46] in order to explore in depth the role of the interactions between the alloying elements in determining the final phases in the microstructure of the Al–Si–Cu–Mg alloys [47] and the extent to which they affect the alloy strength. Based on these studies, zirconium (Zr) will also be added to the base alloy containing 9%Si–2%Cu, 0.6%Mg, 0.15%Fe, followed by Ni addition, to study the combined effect of Zr on the strength properties of the 354 alloy at ambient and high temperatures. Transmission electron microscopic analysis will be used to monitor the changes in the size, density, and distribution of the precipitates formed and their crystallographic characteristics.

2. Experimental Procedure

The Al–Si–Cu–Mg base alloy was received in the form of ingots (13 kg each). Alloying elements were added using Al–25%Ni, Al–20%Zr, Al–11%Sr, and Al–5%Ti–1%B master alloys, as well as pure silver (Ag), to the molten commercial base alloy to produce the four compositions listed in Table 1. Before casting, the melt temperature was $\sim 750 \pm 5^\circ\text{C}$. For each alloy prepared, the molten bath was degassed for about 20 min with a graphite impeller turning at a speed of ~ 130 rpm, applying argon gas. Samplings for chemical composition were carried out prior to casting. The chemical analysis was done using a spectral analysis technique. The chemical analysis was carried out using a Spectrolab-JrCCD Spark Analyzer (Spectro Analytical Instruments inc., Mahwah, NJ, USA). The average chemical composition is three burns per alloy sample. The average chemical compositions (three burns per alloy sample) are reported in Table 1.

Table 1. Chemical analysis (wt%) of the alloys used in the present study.

Alloy Code	Elements (wt%) *,**									
	Si	Cu	Mg	Fe	Ti	Zr	Ni	Ag	Sr	Al
B	8.5	2.0	0.59	0.15	0.15	0.35	0.1	0.68	--	Bal
BS	8.6	1.8	0.48	0.15	0.18	0.23	0.1	0.67	0.017	Bal
B2N	8.5	1.8	0.58	0.13	0.18	0.23	2.0	0.68	0.015	Bal
B4N	8.7	1.9	0.68	0.2	0.20	0.30	4.0	0.72	0.017	Bal

* All alloys contain about 0.06%Sc to enhance grain refining; ** Major elemental differences in the alloys.

Thereafter, the melt was cast into a preheated (450 °C) metallic mold—Figure 1. This mold is characterized by a large liquid metal entry (riser) that will accommodate the shrinkage cavity, resulting in a sound, uniform long bar with a square cross section. Another set of castings was prepared using an ASTM B-118 type permanent mold (gage length coated with a thin layer of ultra-fine boron-nitride). The mold was preheated at 450 °C, and the solidification rate was estimated at 7 °C/s. All prepared samples were heat treated using an air circulation electrical oven. Details of the applied heat treatments will be mentioned further on in the text.

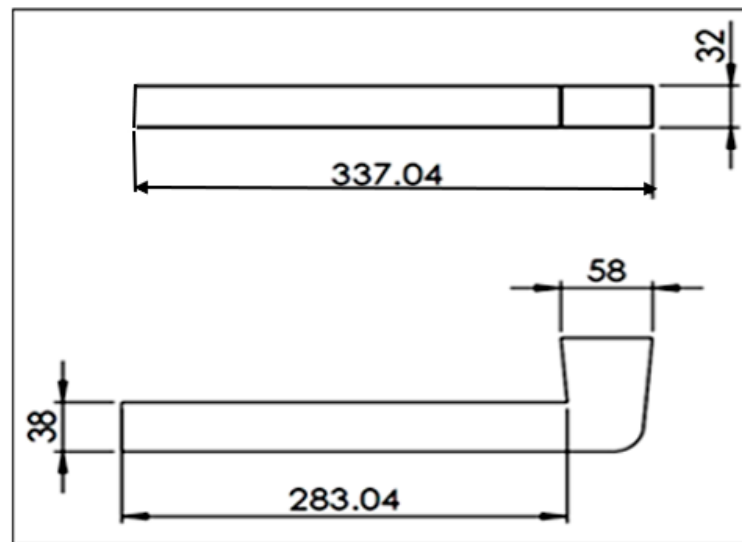


Figure 1. L-shape casting mold (all dimensions are in mm; solidification rate was ~ 3 °C/s).

The heat treatment was carried out using a Lindberg Blue M electric furnace (Thermo Fisher Scientific, Waltham, MA, USA). It is important to mention that the time elapse between removal of the test-bar bundles from the furnace and quenching was at most ~ 5 s. Tensile bars were solutionized at 511 °C for 8 h, followed by quenching in warm water (60 °C). Table 2a,b summarizes the applied working conditions.

Following heat treatment, all tensile test bars were pulled to fracture at ambient temperature (and an MTS servo-hydraulic mechanical testing machine) at a strain rate of $4 \times 10^{-4} \text{ s}^{-1}$. An attachable extensometer (strain gauge) was used to measure the deformation that took place in the samples during deformation, where the data acquisition system attached to the machine converts it to an accurate measure of the percentage elongation. The data acquisition system provides the tensile properties in terms of ultimate tensile strength (UTS), yield strength (YS), and the percentage elongation to fracture (%El). Five test bars for each alloy/condition were tested, and the average values of ultimate tensile strength (UTS), 0.2% offset yield strength (YS), and percentage elongation to fracture (%El) were reported as representing the tensile properties of the corresponding alloy/condition. Some of these bars were tested at 240 °C [48].

A high-sensitivity Type-K (chromel–alumel) thermocouple, which has to be insulated using a double-walled ceramic tube, is attached to the center of the graphite mold. The temperature–time data is collected using a high-speed data acquisition system linked to a computer system to record the temperature-time data every 0.1 s [43]. From this data, the solidification curves and the corresponding first derivative curves for a number of selected alloys were plotted to identify the main reactions occurring during solidification with the corresponding temperatures. The various phases, which constitute the microstructure of each alloy, were expected to be revealed as well. The solidification rate determined from the dendrite arm spacing is about 0.8 °C/s.

Table 2. Details of the applied heat treatments.

(a)		
Treatment #	Description	
1	AC	
2	AC + 8 h/240 °C	As cast (AC) T5
3	AC + 110 h/240 °C	
4	AC + 200 h/240 °C	
5	SHT + 8 h/240 °C	Solution heat treatment (SHT) 495 °C/5 h/quenching in warm water (60 °C) T7
(b)		
Treatment #	Description	
1	AC	
2	AC + 8 h/240 °C	As cast (AC) T5
3	AC + 110 h/240 °C	
4	AC + 200 h/240 °C	
5	SHT + 8 h/240 °C	Solution heat treatment (SHT)
6	SHT + 50 h/240 °C	495 °C/5 h/quenching in warm water (60 °C) T7
7	SHT + 110 h/240 °C	
8	SHT + 200 h/240 °C	

Vickers hardness measurements were carried out using an automatic CLEMEX micro-hardness tester (Brossard, Montreal, QC, Canada), and an indentation load of 110 gf was applied for 11 s. Sixteen indentations were made on each specimen to analyze the hardness distribution. Scanning electron microscopic (SEM) analysis was carried out employing a Hitachi SU-8230 FESEM (Chiyoda City, Japan) equipped with a Bruker Quantax Flat Quad EDS detector (Madison, WI, USA) to investigate phase evolution in the heat-treated and reference samples. Transmission electron microscopy (TEM) was used employing a FEI Tecnai G2 F20 electron microscope (Sensitive Instrument Facility, Ames, IA, USA), equipped with an advanced control system that permits the integration of an EDAX™ chemical analysis system, and scanning transmission electron microscopy (STEM). The microscope was operated at an accelerating voltage of 20 kV.

The preparation process of samples for high-resolution transmission electron microscopy includes sectioning a very thin disc of about ~300 µm from the original thick samples that were solidified at a rate of 0.35 °C/s. In order to avoid mechanical deformation of the disc, cutting was carried out using a diamond disk at a low speed. Thereafter, 3-mm diameter discs were prepared from the thinned discs. In order to further thin the prepared foils, an UniMill IV7 ion milling machine (Technoorg Linda Co., Limited, Budapest, Hungary) was employed to produce transparent foils.

The main purpose of applying the DSC analysis system was for identification of the phases that were precipitated during the solidification process at a rate of 0.355 °C/s. The main purpose of using such a low solidification rate was to increase the solidification time and hence the size of the precipitated phase in order to obtain more accurate and reliable data. The thermal analysis method (DTA analysis) was carried out in the same manner the 354 alloy heats were prepared. In this case, the initial materials were melted in a 2-kg SiC crucible by means of an electrical furnace at 750 °C, then poured in a graphite crucible pre-heated at 600 °C. As a result, a solidification rate of about 0.35 °C/s could be achieved.

3. Results and Discussion

3.1. Microhardness and Tensile Testing

Figure 2 shows the effect of Sr and Ni addition on the aging behavior of the 354 alloy in the temperature range of 160–240 °C and for aging times varying from 0 to 50 h, with 0 h representing the T4 heat treatment. The samples were solutionized at 495 °C for 5 h prior to quenching in warm water (60 °C); 0 h corresponds to T4) [48–50].

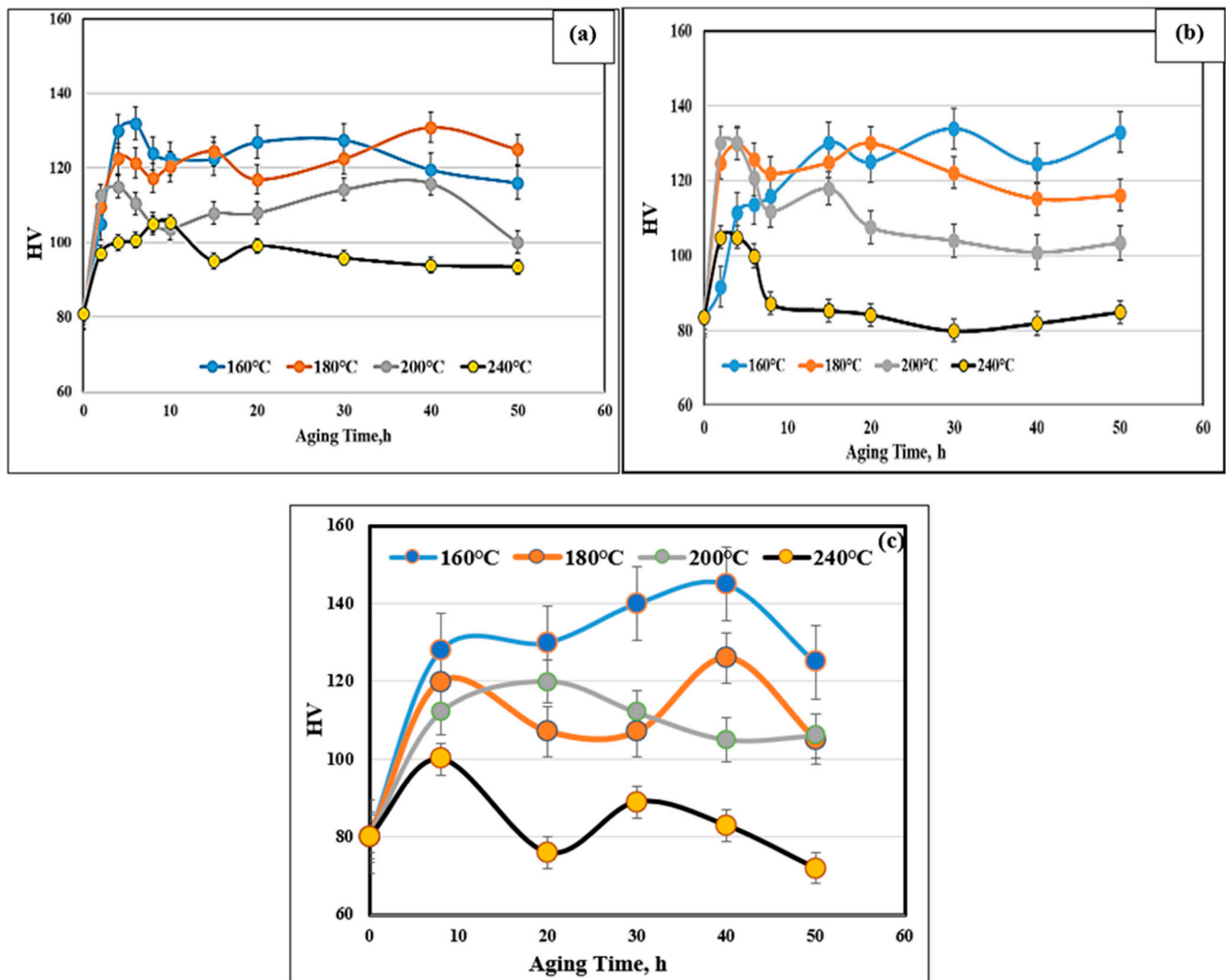


Figure 2. Variation in microhardness of (a), B (b) BS, (c) B2N alloys as a function of aging temperature and time.

Abdelaziz et al. [48] performed a series of aging treatments on 319 alloy containing 6.8%Si-3%Cu-0.3%Mg. The results revealed that all hardness curves exhibited wavy patterns composed of multiple peaks, whereas the 356 alloy (containing 7%Si-0.35%Mg) revealed only a single peak. Zhou et al. [49] confirmed the observations made on the 319 alloy. Mohamed et al. [50] interpreted the results in terms of the precipitation of Al_2Cu and Al_2CuMg phase particles as well as the increased bonding of the Si particles with the matrix, where the thermal energy is sufficient to precipitate such hard phases. The growth of the phase precipitates with an increase in the aging time, which would cause softening. The hardness measurements presented in Figure 2a,b show the clear lack in the start of hardening for the BS alloy at 160 °C.

Joeno and Gruzleski [51] reported that in Mg-containing alloys (Mg > 1%), it is likely that Sr would react with Mg, forming the $\text{Mg}_2\text{SrAl}_4\text{Si}_3$ phase, which precipitates prior to

the eutectic reaction; this would explain the occurrence of such aging behavior. Another point to emphasize is the fast particle coarsening rate on aging at 240 °C exhibited by the BS alloy compared to that shown by the B alloy, which may be attributed to a lack of free Mg, resulting in a lesser number of strengthening precipitates.

The microstructure shown in Figure 2c for the B2N alloy reveals a large volume fraction of Ni-based phases. Whereas it is known that Cu and Ni can dissolve in each other, producing Cu–Ni compounds that are insoluble in the surrounding Al matrix (marked X). Figure 3a depicts the variation in the ultimate tensile strength (UTS) of the three studied alloys (i.e., BS, B2N, and B4N) following different aging treatments as described in Table 2a. As can be seen, the highest resistance to softening is associated with alloy B4N in the T5- and T7-treated conditions. The lowest values were obtained in the T5- and T7-treated conditions for BS and B2N alloys.

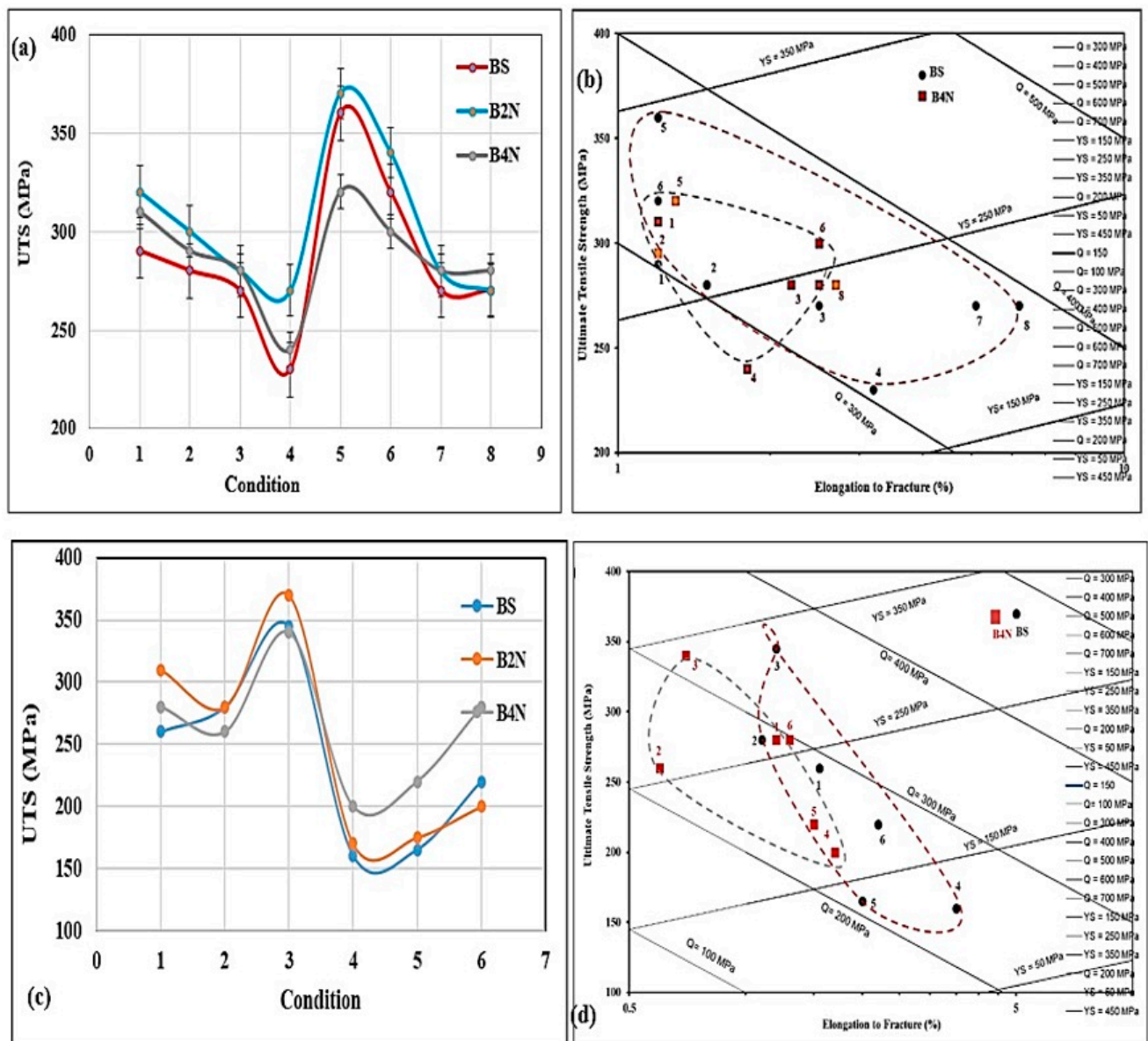


Figure 3. Variation in the alloy tensile properties as a function of the applied heat treatment and testing temperature: (a) ultimate tensile strength (Table 2a)—RT, (b) Q-chart of data in (a), (c) ultimate tensile strength (Table 2b)—240 °C, (d) Q-chart of data in (c). The conditions 1 to 8 and 1 to 6 marked on the X-axis in (a,c) refer to the heat treatment conditions listed in Table 2. The dashed lines in (b,d) outline how the quality and strength of the alloy evolves with the heat treatment conditions.

The T7-treated B2N and B4N alloys, with 2 and 4 wt% Ni, respectively, show the best strength values after 200 h aging at 240 °C following solutionizing at 495 °C for 5h. This observation may be interpreted in terms of the simultaneous precipitation of Al–Cu–Ni and Al₃Ni phases in all Ni-containing alloys (B2N, B4N). In particular, alloy B4N reveals the best resistance to softening and highest strength values, likely due to the uniform distribution of (Al–Al₃Ni) eutectic structure. These observations are better represented by the quality index chart following the concept proposed by Drouzy et al. [52] and Jacob [53], as shown in Figure 3b for the BS and B4N alloys. It is evident from Figure 3b that the data for the BS alloy, expands over an area almost twice that of the B4N alloy, where all spots are seen to fall in clusters. However, at prolonged aging at 240 °C, alloy B4N offers better resistance to softening compared to that produced by the BS alloy.

Table 2b lists the heat treatment conditions of alloys tested at 240 °C. From Figure 3c, it may be seen that testing at 240 °C resulted in a noticeable reduction in both YS and UTS strength parameters compared to the values obtained at room temperature. On the other hand, as Figure 3b reveals, increased values of ductility were obtained when testing at 240 °C, compared to those reported from ambient temperature tests. These observations may be attributed to the softening associated with tensile testing at high temperatures, consequent to coarsening and subsequent reduction in density of the main strengthening precipitates, e.g., Al₂Cu, Mg₂Si, and Al₂CuMg.

One of the main advantages of Ni addition is the improvement in alloy resistance to softening at high-temperatures, i.e., 240 °C [54]. In the present work, alloy B4N exhibited the highest resistance to softening during high temperature testing. In the T7-treated condition, alloy B4N (containing 4 wt% Ni) exhibited a reduction in YS by about 65 MPa when tested at 240 °C. In comparison, alloy B2N (with 2 wt% Ni) displayed the lowest resistance to softening, with a loss in YS of about 140 MPa. The high resistance to softening at 240 °C shown by alloy B4N may be attributed to precipitation of fine Al₃Ni phase (Al–Al₃Ni) with the increase in Ni-content from 2 to 4 wt% Ni. It is well documented that a finely distributed Al₃Ni phase, e.g., as that observed in alloy B4N, would enhance the elevated temperature strength significantly compared to its coarsened size observed in the microstructures of the 2 wt% Ni-containing B2N alloy [55,56].

The quality index values of the BS and B4N alloys are depicted in Figure 3d following the concept of Drouzy et al. [52] for selected heat treatment conditions as described in Table 2. Both alloys revealed a marked drop in Q-values at 240 °C due to a major reduction in the corresponding UTS levels despite their improved ductility values. The Q values of alloy B4N are low, in general, except for the Q value for the T7-treated condition when tested at 240 °C due to the noticeably increased strength of alloy B4N at this temperature. Table 3 lists the Reactions 1 through 8 and the corresponding phases and reaction temperature ranges observed for the base alloy B (or BS) and B2N based on ref. [57].

Table 3. Main reactions taking place during solidification of alloys B and B2N [57].

Reaction #	Suggested Temperature Range (°C)	Suggested Precipitated Phase
1	600–597	Formation of α -aluminum dendritic network
2	560–558	Precipitation of Al–Si eutectic Precipitation of post-eutectic β -Al ₅ FeSi phase
3	555–556	Precipitation of Al ₉ FeNi phase
4	540–538	Precipitation of Mg ₂ Si phase
5	525–523	Transforming of β -phase into π -Al ₈ Mg ₃ FeSi ₆ phase
6	523–520	Precipitation of Al ₃ CuNi phase
7	500–496	Formation of eutectic Al–Al ₂ Cu phase
8	485–489	Precipitation of Q–Al ₅ Mg ₈ Cu ₂ Si ₆ phase

The fractured surface of T7-treated alloy BS after testing at room temperature, seen in Figure 4a, displays a fine dimple structure together with bright $\text{Al}_x(\text{Zr, Ti})\text{Si}$ precipitates. The inset shows the EDX of these precipitates; some of them appear in star-like form. The high temperature-tested sample of the alloy shows a cracked $\text{Al}_x(\text{Zr, Ti})\text{Si}$ particle (arrowed) in the high magnification image displayed in Figure 4b. Several fine precipitates of mostly Al_2Cu particles are also observed, bordering the block-like $\text{Al}_x(\text{Zr, Ti})\text{Si}$ particle in the figure.

Figure 4c,d display the fracture characteristics of the T7-heat-treated alloy B4N when tested, respectively, at ambient and high temperatures. Large Ni-rich phase particles are observed in both cases. The EDS spectrum taken from the spot X in Figure 4c shown in the inset indicates that these are Al_3Ni particles. The black arrows in the figure point to their fractured nature, while the brittle nature of the alloy is evidenced by the finely dimpled network surrounding the Al_3Ni particles. As Table 7 indicates, while high temperature testing hardly increased the volume fraction or size of the Ni-based phases (Figure 4d), the size of the dimple structure was noticeably bigger (see inset micrograph). However, any improvement due to the increased aluminum matrix area was offset by the high-volume fraction (about 11.5%—Table 7) of brittle intermetallics present, in addition to precipitation that may have occurred during testing as can be seen at the bottoms of the dimples (inset micrograph—orange arrow).

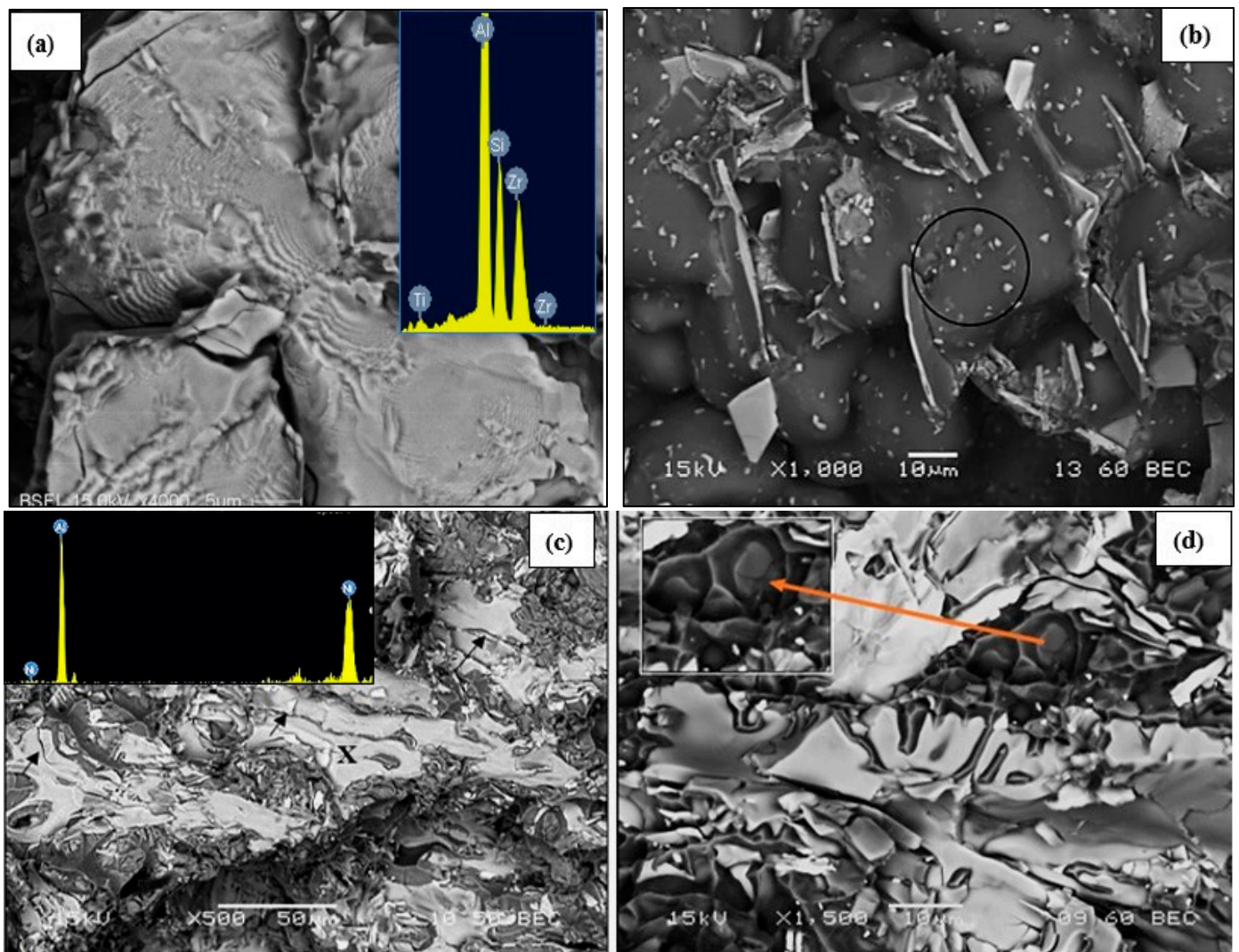


Figure 4. Cont.

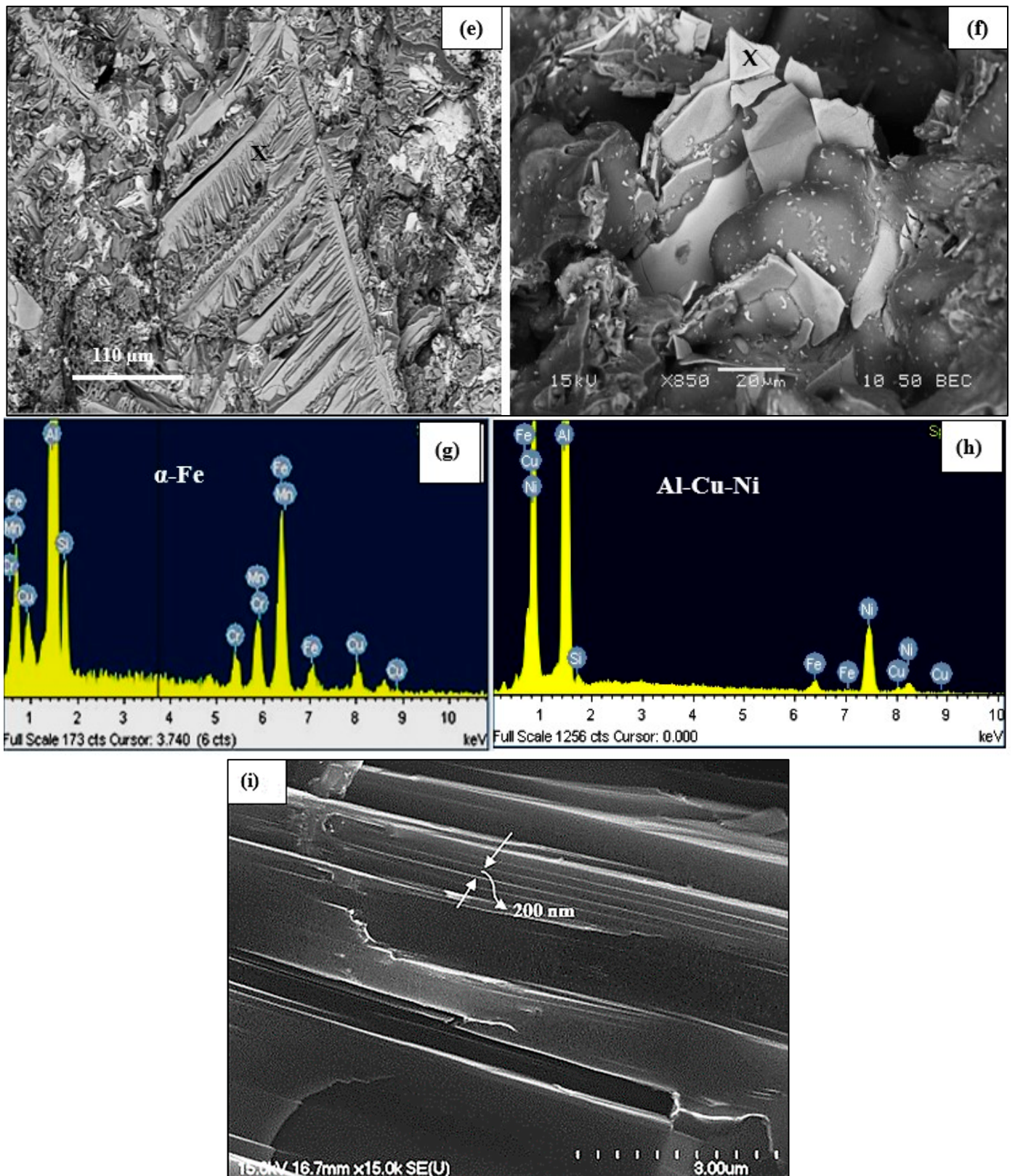


Figure 4. Fracture surface of BS alloy in the T7 condition, tested at: (a) 25 °C, (b) 240 °C; fracture surface of the B4N alloy in the T7 condition, tested at: (c) 25 °C, (d) 240 °C—note the precipitation of Ni-rich phase particles in the form of dendritic cells; (e,f) precipitation of (e) α -Fe and of Al_2Cu phase particles; (g,h) EDS spectra corresponding to areas marked X in (e,f), respectively; (i) stacking faults.

Consider the atomic numbers of Fe, Ni, and Zr: 26, 28, and 40, respectively. The backscattered electron image presented in Figure 4e reveals the fracture of α -Fe in its dendritic shape similar to that featured in Figure 4d except for its grayer color when compared to the bright appearance of the Ni-based intermetallic phase due to the obvious difference in the atomic numbers of the two phases. The fracture surface depicted in Figure 4f demonstrates two main observations: the presence of the Al–Ni–Cu phase in the form of platelets coupled with a large density of fine Al₂Cu particles. Since it is a fracture surface, it is difficult to estimate the density of the precipitates. Figures 4g and 4h are the EDS spectra corresponding to Figures 4e and 4f, respectively, obtained from the spots marked X in each case. Occasionally stacking faults were seen in the fracture surface, as displayed in Figure 4i.

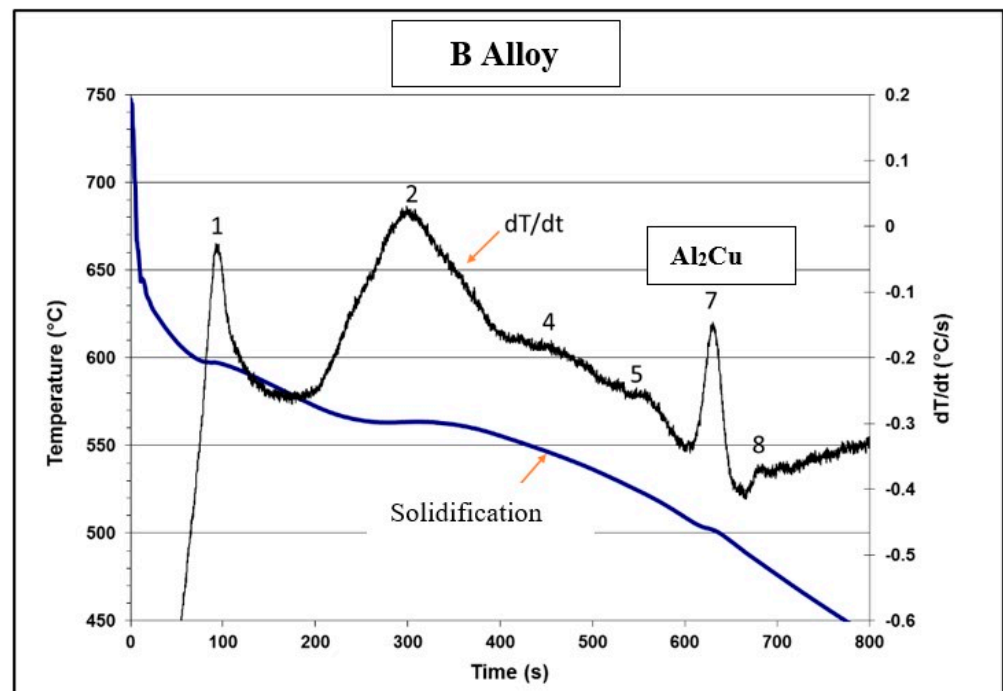
3.2. Microstructural Characterization of As-Cast Alloys

3.2.1. Thermal Analysis

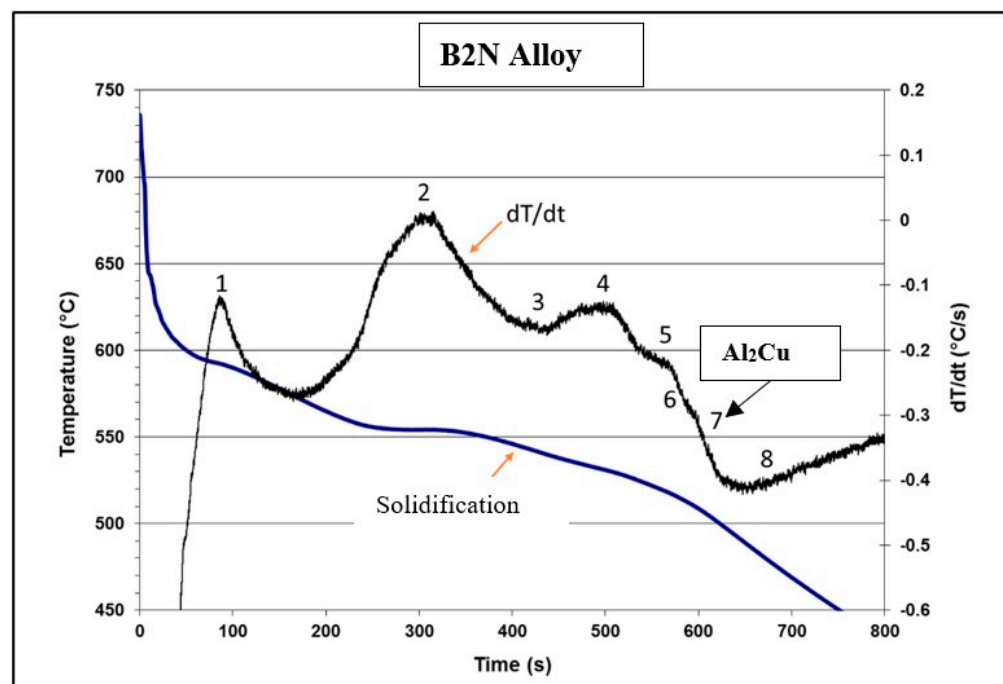
The base alloy B is an Al–Si–Cu–Mg alloy, with its composition of 8.4 wt%Si, 0.15 wt%Fe, 2.1 wt%Cu, 0.59 wt%Mg, and 0.15 wt%Ti. It is expected that Cu-rich, Mg-rich, and Fe-rich intermetallic phases will mainly precipitate during solidification. Referring to Table 3, which lists reactions expected in such alloys, and as seen from Figure 5a, solidification commences at 598 °C with the formation of the dendritic Al network (reaction 1), followed by the Al–Si eutectic at 560 °C and post-eutectic B–Al₅FeSi phase (reaction 2), Mg₂Si at 540 °C (reaction 4), and the beta-Fe to pi-Fe phase transformation at 525 °C. Finally, precipitation of the Al₂Cu and Q–Al₅Mg₈Cu₂Si₆ phases occurs at 498 °C and 488 °C when solidification is completed. The WDS analysis of the reported phases is listed in Table 4.

Table 4. WDS analysis of phases reported in alloy B.

Alloy Code	Element	at%	Calculated Formula	Suggested Formula
B	Al	51.51	Al _{11.6} Fe ₆ Mg _{4.02} Si _{4.7}	π -Al ₈ Mg ₃ FeSi ₆
	Fe	4.85		
	Mg	19.53		
	Si	23.12		
	Total	99.01		
	Al	68.11	Al _{2.25} Cu	Θ -Al ₂ Cu
	Cu	30.21		
	Total	98.31		
	Mg	11.14	Al _{4.08} Cu ₂ Mg _{9.2} Si ₇	Q-Al ₅ Mg ₈ Cu ₂ Si ₆
	Al	47.41		
	Si	8.70		
	Cu	33.74		
	Total	100.00		
	Mg	24.82	Mg _{2.1} Si	Mg ₂ Si
	Al	45.23		
Si	21.98			
Cu	7.97			
Total	100.1			



(a)



(b)

Figure 5. Cont.

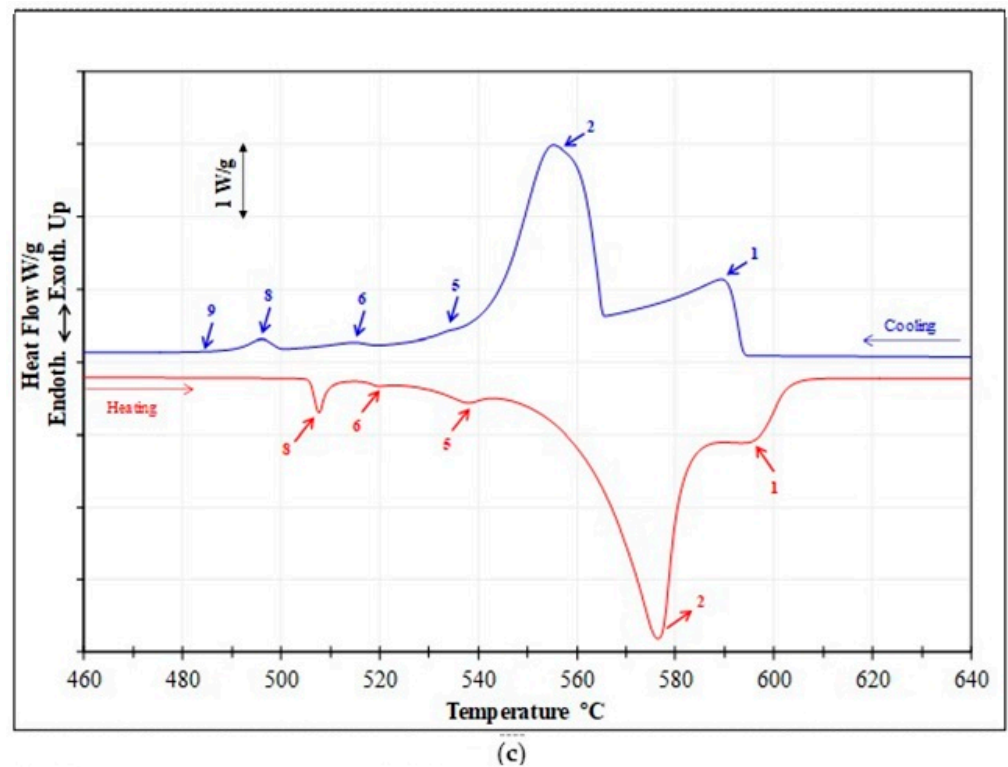


Figure 5. (a) Solidification curve (blue) and its first derivative (black) obtained from alloy B. (b) Solidification curve (blue) and its first derivative (black) obtained from alloy B2N (containing 2 wt% Ni + 0.25 wt% Zr). (c) DSC solidification curves of the BS alloy (see Table 6 for reactions).

The solidification curve for alloy B2N containing 2 wt% Ni + 0.25 wt% Zr is shown in Figure 5b. Table 5 presents the chemical compositions of the phases examined in alloy B2N as obtained from the WDS analysis of the sample used. Note the disappearance of reaction #7 (precipitation of Al_2Cu) in Figure 5b.

Table 5. WDS analysis of phases observed in alloy B2N.

Alloy Code	Element	wt%	at%	Calculated Formula	Suggested Formula
	Al	37.67	58.41	$\text{Al}_{5.88}\text{Si}_{1.34}\text{Ti}_{0.25}\text{Zr}_{2.14}$	$(\text{Al,Si})_3(\text{Ti,Zr})$
	Si	11.94	16.29		
	Ti	3.79	3.31		
	Zr	47.14	21.62		
	Total	99.54	99.63		
B2N	Al	66.69	80.44	$\text{Al}_{8.94}\text{Fe}_{0.25}\text{Ni}_{1.7}$	$\text{Al}_9(\text{FeNi})$
	Fe	3.86	2.25		
	Ni	27.62	15.31		
	Total	99.85	98.86		
	Al	40.77	61.03	$\text{Al}_{3.30}\text{Ni}_{1.13}\text{Cu}$	Al_3CuNi
	Ni	29.77	20.48		
	Cu	28.44	18.07		
	Total	98.98	99.58		

DSC solidification and melting curves of the base BS alloy studied are provided in Figure 5c, displaying the suggested endothermic and exothermic transformation reactions. These reactions are listed in Table 6.

Table 6. Suggested reactions taking place during solidification/melting of the BS alloy [24,54,57].

Reaction #	Transformation Temperature (°C) [24,54,57]	Reactions Occurring during Solidification and Melting	Temperatures Reported during Solidification (°C)	Temperatures Reported during Melting (°C)
			BS	BS
1	600–597	α -Al dendritic network	590	595
2	560–558	Al-Si eutectic Post-eutectic β -Al ₅ FeSi phase α -Al ₁₅ (Fe,Mn) ₃ Si ₂ phase for Mn-containing alloys	556	576
3	555–556	Al ₉ FeNi phase	-	-
4	546–553	Al ₃ Ni phase	-	-
5	540–538	Mg ₂ Si phase	534	538
6	525–523	Transformation of β to π -Al ₈ Mg ₃ FeSi ₆ phase	516	520
7	523–520	Al ₃ CuNi phase	-	-
8	500–496	eutectic Al-Al ₂ Cu phase	496	507

3.2.2. Optical and SEM Investigations of as Cast Alloys

While the literature reports many studies on the effects of Ni addition to Al–Si alloys [55–58] in relation to the microstructure/mechanical properties, most of them are focused on Ni-phase precipitates, neglecting other aspects such as grain refining, for example. In the present study, a certain amount of grain refining was observed in the B2N alloy (15–20%), much less than that anticipated with 2% Ni addition. Wangi and Reif [58] attribute this refining to the constitutional undercooling effect of Ni.

Table 7 lists the volume fraction of undissolvable intermetallics in the present alloys in the as-cast condition and after quenching from the solutionizing temperature (T4 tempered condition). Taking into consideration that all alloys (except the B (or BS) base alloy) contain about 150 ppm Sr, Figure 6 compares the changes in the microstructure of BS and B2N alloys in the as-cast condition. It is observed that Ni may lead to some Si particle refinement as seen in the circled areas but not enough to classify Ni as a grain refiner similar to that obtained using approximately 0.1–0.2%Ti in the form of Al₃Ti [59] or TiB₂ [60–65].

Table 7. Volume percentage (%) of undissolved phases in as-cast and T4-tempered alloys.

Condition	Volume Fraction (%)			
	Alloy	B	B2N	B4N
As cast		2.5 ± 0.4	12.2 ± 0.8	15.3 ± 0.8
T4		1.2 ± 0.3	9.5 ± 0.7	11.5 ± 0.6

Garza-Elizondo et al. [66] reported that the as-cast microstructure of 354 alloy consists of dendrite arm spacings (DAS) in the range 50–70 μ m using a close-to-equilibrium solidification rate, which was also used in the present work. Figure 7a shows the microstructure of the as-cast BS alloy, revealing the precipitation of a large volume of Al₂Cu phase particles surrounded by well-modified eutectic Si particles. The associated EDS of the area marked X in Figure 7c reveals a strong peak due to Mg, indicating the possibility of the precipitation of Q-Al₅Cu₂Mg₈Si₆ phase [67–69], as listed in Table 3 and shown in the inset micrograph at the top left in Figure 7a.

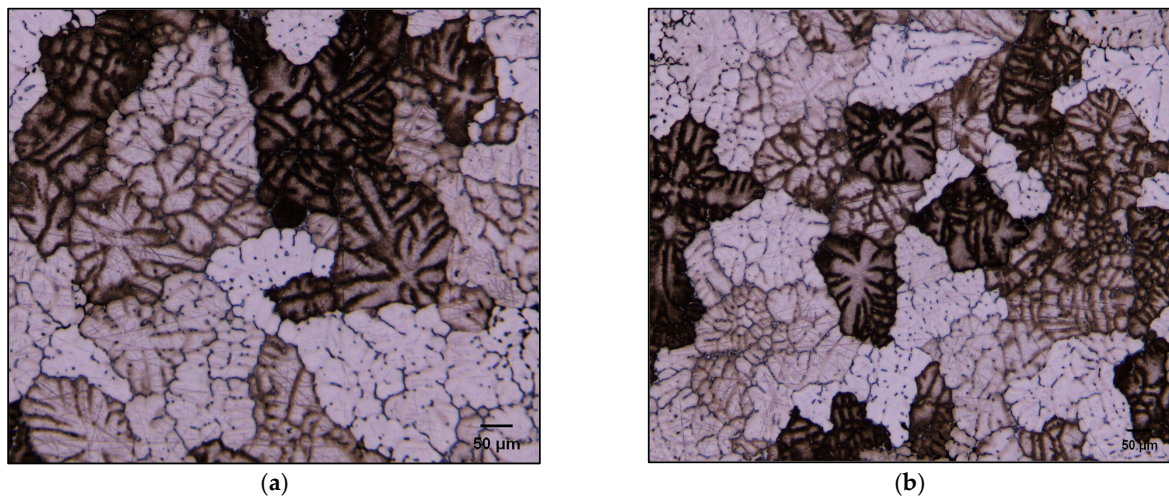


Figure 6. Macrostructure of grains in the as-cast: (a) B alloy, (b) B2N alloy. Samples were lightly etched to reveal the secondary dendrite arm spacing (SDAS).

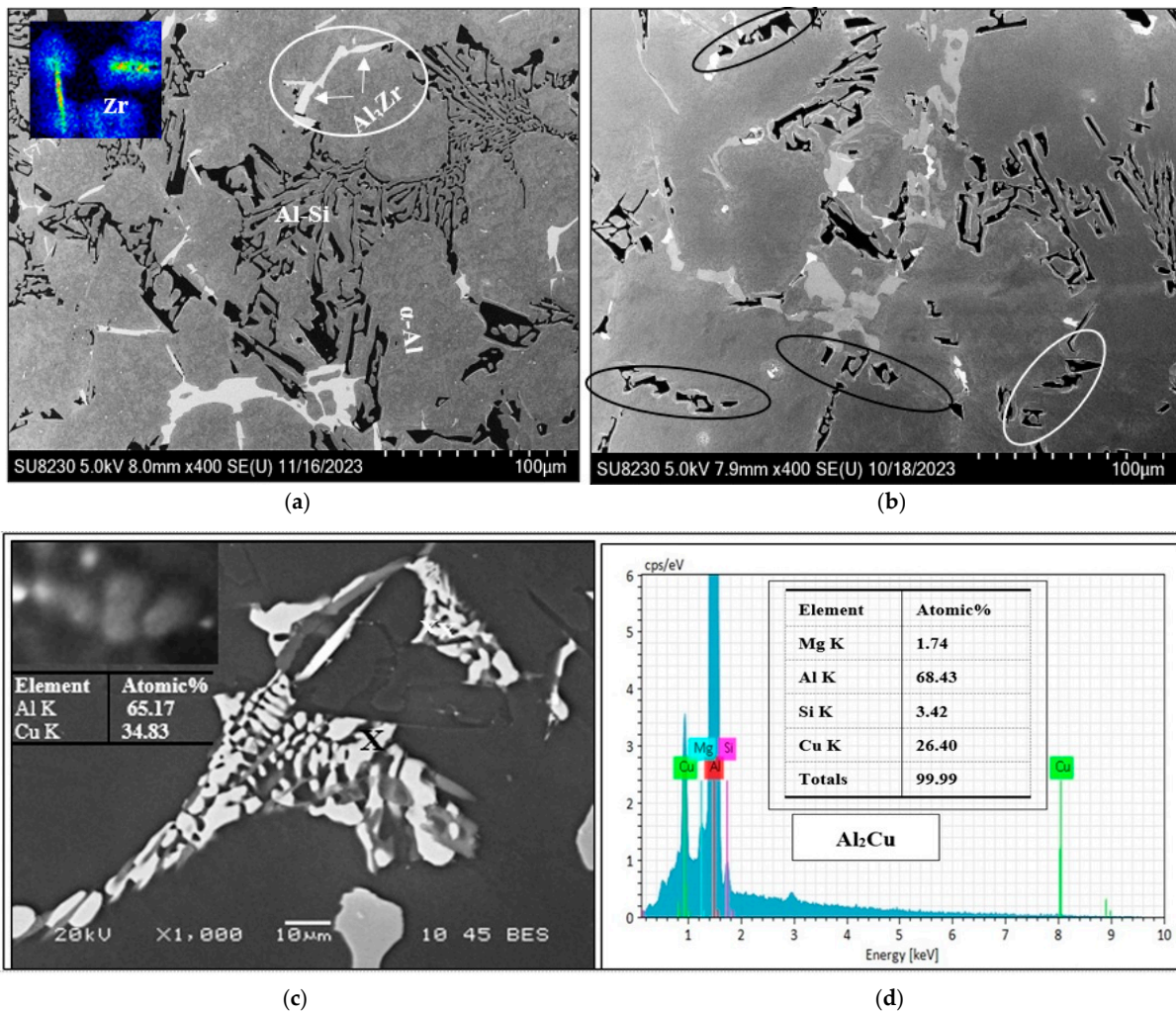


Figure 7. Backscattered electron micrographs of (a) BS and (b) B2N alloys in the as-cast condition revealing precipitation of Al₃Zr and eutectic Si phase particles in BS alloy—white circled area in (a), and eutectic Si particles in B2N alloy—see the white or black circles in (b); (c) Backscattered electron micrograph of BS alloy in the as-cast condition; (d) EDS spectrum corresponding to the white area in (c) marked X.

Garza-Elizondo and coworkers [66] reported that in the 354 alloy they investigated, the as-cast structure displayed DAS or dendrite arm spacing values of 50–70 μm when the alloy was solidified under equilibrium solidification conditions. Such conditions were also adopted in the present study. The as-cast microstructure of the BS alloy displayed in Figure 7a shows a large amount of Al_2Cu precipitates surrounded by fine Al–Si eutectic regions. The EDS spectrum taken from X in Figure 7c, depicting a concentrated region of Al_2Cu particles in the alloy, also exhibits a peak due to Mg, which indicates the possible presence of the Q- $\text{Al}_5\text{Cu}_2\text{Mg}_8\text{Si}_6$ phase, as listed in Table 3 and shown in the inset micrograph at the top left in Figure 7c.

It may be inferred from the Al–Zr binary phase diagram that the melting temperature of Al–0.3% Zr is about 750 $^\circ\text{C}$. Therefore, in the present work, the temperature of the melt was raised to 820 $^\circ\text{C}$ to allow for the dissolution of Zr. Thereafter, the temperature was lowered to 750 $^\circ\text{C}$ before starting the degassing process. During solidification and before reaching the peritectic reaction at 660 $^\circ\text{C}$, primary Al_3Zr particles would precipitate in the form of dispersoids [70–72]. Figure 8a shows that in the B2N alloy, it is possible that Al–Ni–Cu compound may precipitate, covering the Al_3Zr particles. In addition, Ni would also react with Zr, forming Ni_5Zr compound [73,74]. On the other hand, Cu would react with both Ni and Zr (Cu_9Zr_2) [75,76]. Figure 8b is the EDS spectrum corresponding to the black rectangular area in Figure 8a, revealing peaks of Al, Ti, Cu, Zr, and Ni, whereas the EDS spectrum obtained from the orange square reveals strong Zr peaks, as seen from Figure 8c.

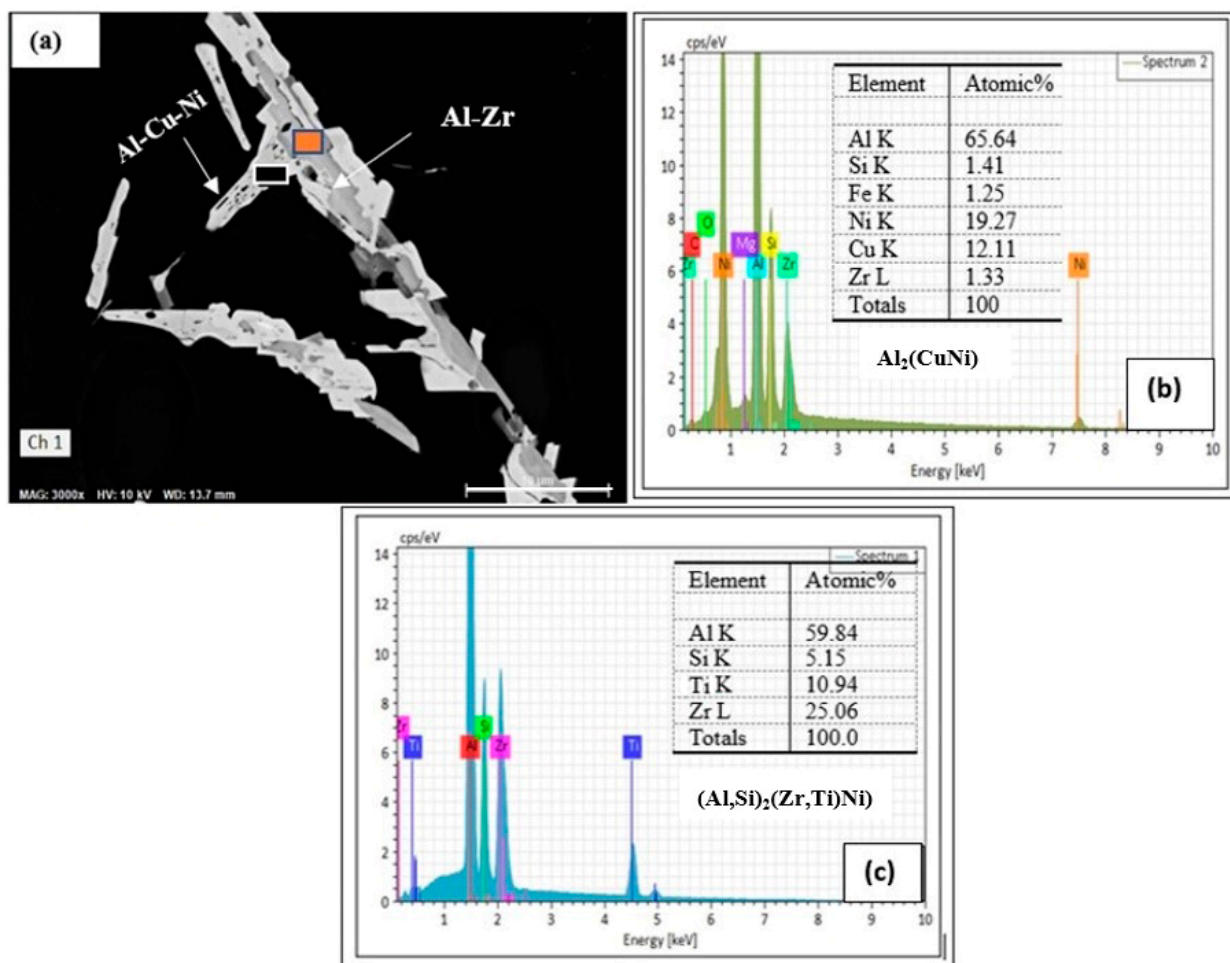


Figure 8. (a) Backscattered electron micrograph of the B2N alloy in the as-cast condition, (b,c) EDS spectra corresponding to the black and orange squares in (a), respectively. The energies of the $L\alpha$ lines of Cu and Ni are very close (0.933 and 0.853 keV, respectively), leading to overlapping of the lines.

Increasing the Ni content to 4% led to dense precipitation of Ni-containing phases, as noted in the backscattered image displayed in Figure 9a. Spot EDS spectra indicated possible precipitation of Al_9FeNi (59 at%Al, 1.5at%Fe, 21.5 at%Ni, 18.2 at%Cu)—see the EDS spectrum shown in Figure 9b, corresponding to the black square in Figure 9a, and simultaneous precipitation of Al_3Ni and Al_3CuNi phases as shown in the EDS of Figure 9c, corresponding to the rectangular area outlined in red in Figure 9a.

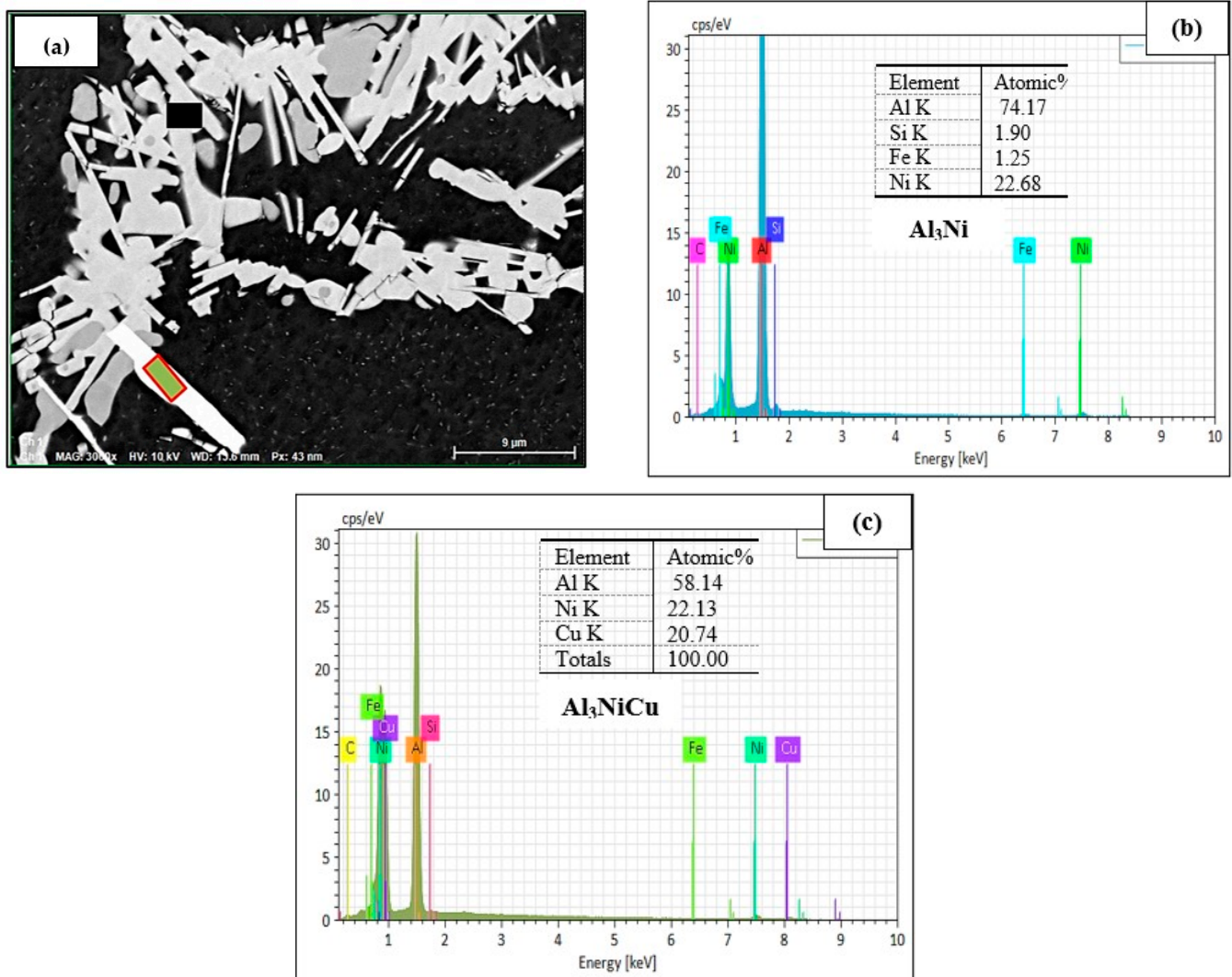


Figure 9. (a) Backscattered electron micrograph of the B2N alloy in the as-cast condition; (b) EDS spectrum corresponding to the black square in (a); (c) EDS spectrum corresponding to the rectangle outlined in red in (a), showing the presence of Al_3Ni , Al_3CuNi phases.

3.3. HR-TEM Analysis

In this section, samples heat-treated in the T6 and T7 conditions will be discussed, in addition to those exposed to a prior stabilizing treatment for 200 h at 240 °C. Figure 10a,b presents the precipitation in samples in the underaged condition (8 h at 160 °C) showing ultra-fine precipitates. These precipitates are still coherent with the aluminum matrix, as inferred from the high-resolution images displayed in Figure 10c,d, revealing contrast-like areas around the coherent precipitates (white arrows). It has been proposed that due to the high degree of coherency, extensive coherency–strain fields are developed, leading to an increase in the peak strength of the alloy. Thus, the formation of θ'' precipitates may lead to distortion in the lattice structure in, and around, their vicinity. These distortions will

impede the movement of dislocations during plastic deformation, resulting in hardening effects [14,22,77–86].

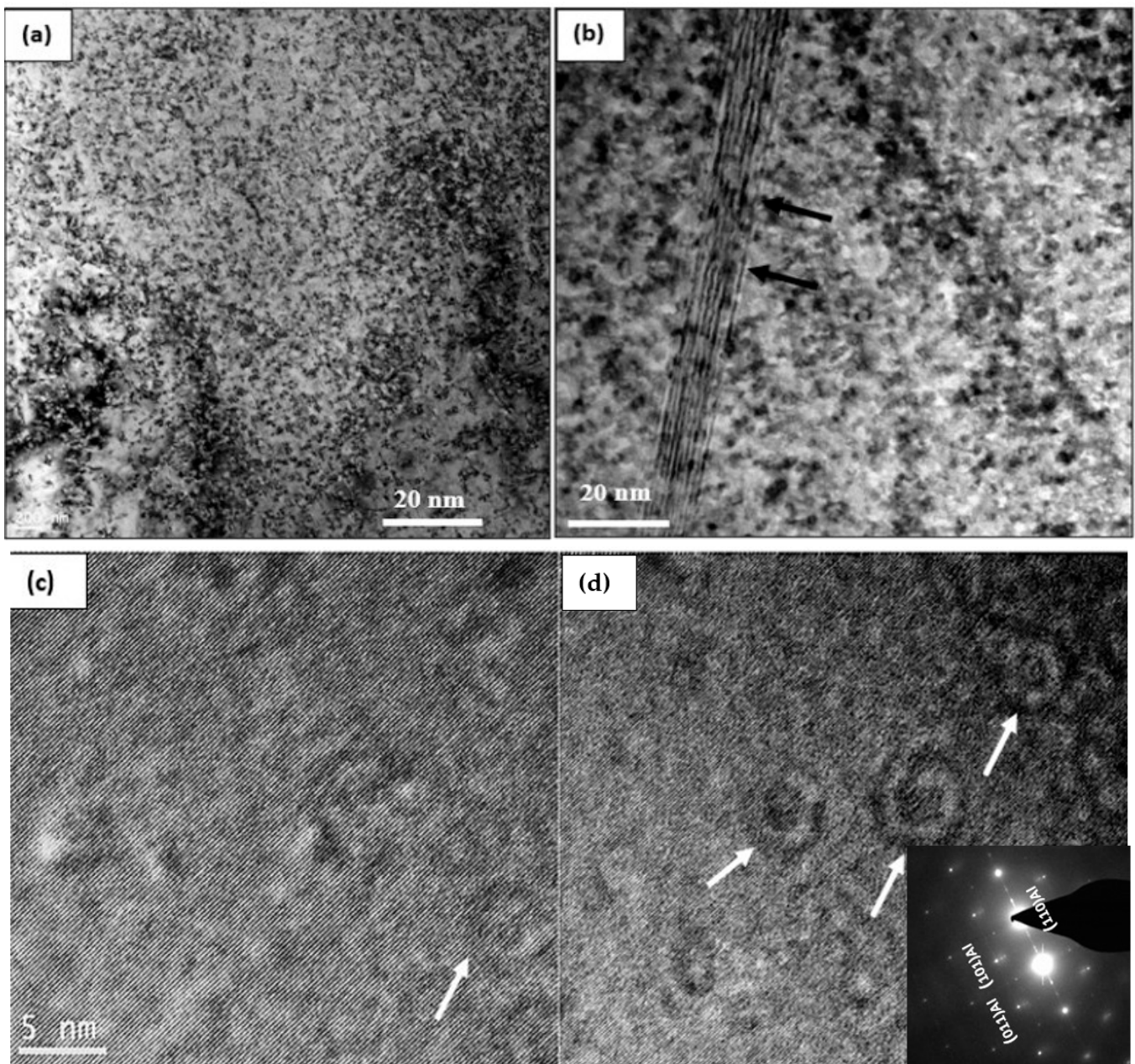


Figure 10. TEM micrographs of the B alloy sample aged for 8 h at 160 °C: (a,b) bright field electron images—note the presence of stacking fault lines in (b) caused by interruption in the order of stacking planes (marked by black arrows); (c) high resolution image showing coherency of the ultra-fine precipitates with the Al matrix; (d) high resolution image of (a)—inset micrograph is SAED-[111]Al zone axis.

Figure 11 reveals further details of the precipitation in the same sample. Figure 11a shows a clearer image of the spherical precipitates (bright field), while Figure 11b shows the corresponding image in dark field mode. The associated selected area electron diffraction (SAED) pattern in the inset micrograph in Figure 11b reveals the presence of small spots (see white circled area) from which Figure 11b was generated, revealing the size and density of the precipitation that occurred during the applied aging treatment.

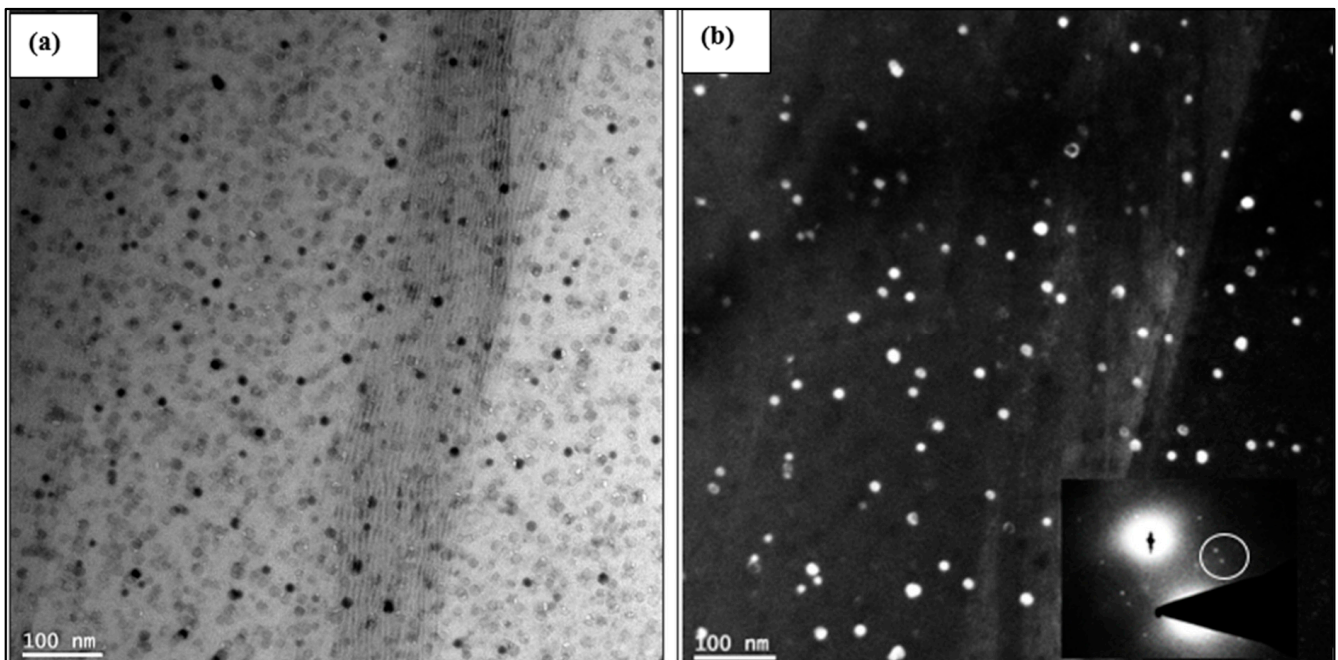


Figure 11. TEM images of the B alloy treated in the T6 tempered condition: (a) bright field, (b) corresponding dark field using double beam.

According to Starke [85] and Weatherly and Nicholson [86], fine θ'' particles would nucleate uniformly, with a strong coherency with the matrix. As a result of this process, strong strain fields similar to those shown in Figure 11a may be generated, resulting in significant enhancement of the alloy strength, as can be seen from Figures 2 and 3. Such lattice structure distortion of the particles, as well as in the surrounding areas of the particles themselves, will restrict displacement of the dislocations, causing the observed hardening effects.

In addition, Starke [85] and Weatherly and Nicholson [86] reported that aging of aluminum alloys at elevated temperatures (overaging) would lead to changes in the microstructure that are independent of applied stress. These changes include the nucleation and growth of new phases as well as a reduction in the dislocation density due to the formation of sub-grains. Furthermore, coarsening of the precipitates may lead to the formation of soft precipitate-free zones along the grain boundaries, thereby disturbing the strength balance across the grains and causing premature crack formation. Thus, during this stage, the applied stresses are expected to enhance the precipitate coarsening rates.

Figure 12a is a bright field micrograph of alloy B aged at 240 °C for 50 h, displaying precipitates in the form of short platelets coarser than those seen in Figure 11a. Figure 12b is a dark field image revealing the presence of various shapes of the precipitated phase particles in the microstructure. It should be mentioned here that these micrographs were prepared from samples following aging with no applied stress. The SAED pattern associated with Figure 12a is shown in Figure 12c. The zone axis is identified as [001]Al. Along the lines, several fine spots could not be identified with certainty. Some concentric rings can also be seen. Due to this difficulty, a colored map was produced, revealing that the large spots in Figure 12a could be identified as Cu-rich particles. The dark field image in Figure 12b was generated using fine spots in the white circles.

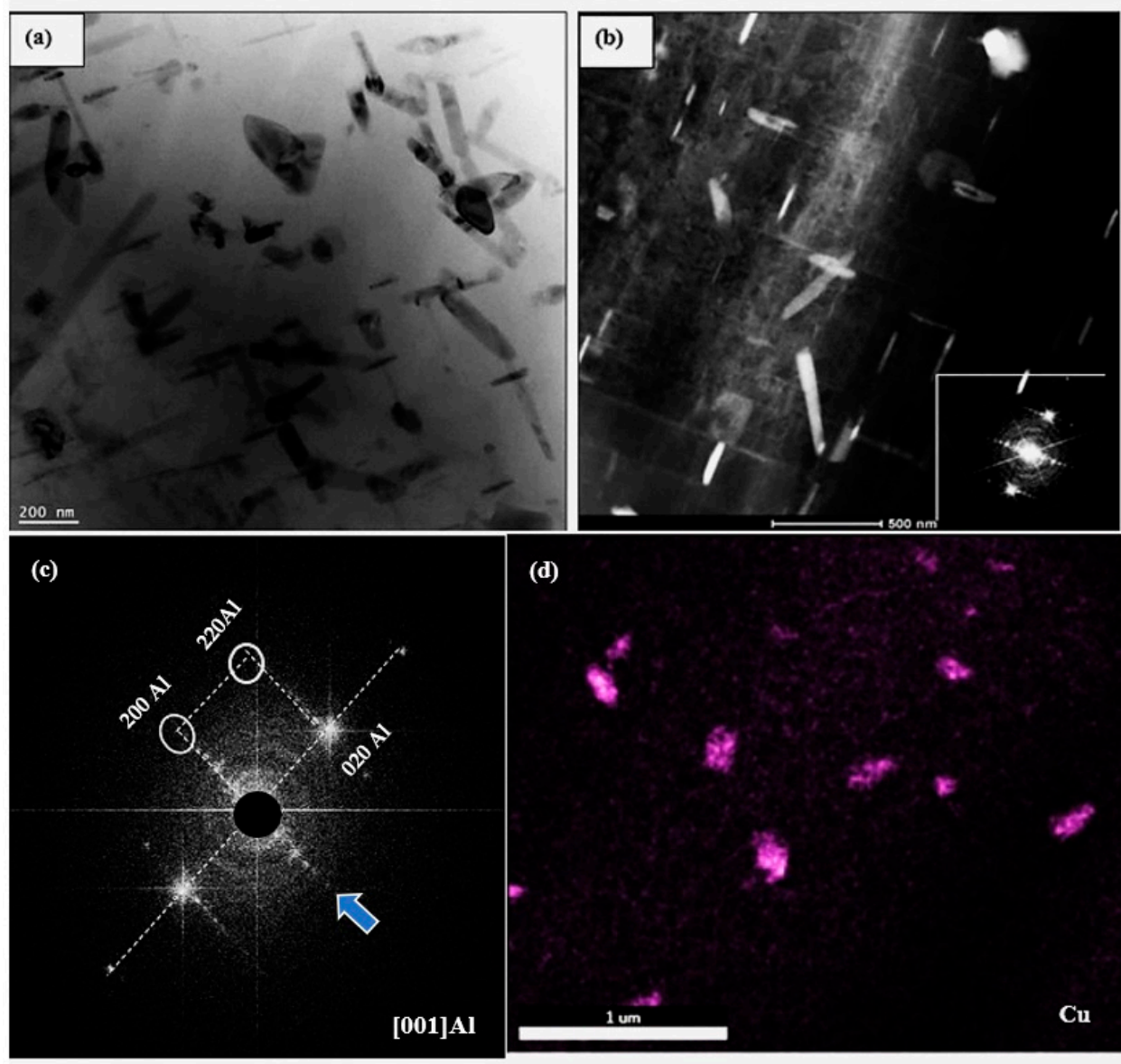


Figure 12. TEM micrographs of the B alloy aged at 240 °C for 50 h: (a) bright field, (b) dark field electron images, (c) the selected area electron diffraction (SAED) pattern obtained from the precipitates in (a)—note the presence of faint white spots (blue arrow). (d) X-ray image of Cu-rich particles in (a).

Several coarsened particles over 200 nm can be seen in the bright-field images presented in composite form in Figure 13a. These particles reveal signs of particles colliding at their interfaces (white arrows) when the aging time at 240 °C was increased to 200 h—note the collision between the particles in the inset micrograph. The dark field image shown in Figure 13b indicates another feature: that is, not all particles have the same zone axis. This statement is supported by the SAED demonstrating several rings formed by a large number of spots. On enlarging Figure 13a, the image in Figure 13c shows interfaces between two colliding particles. Another point to be considered is the presence of dislocation arrays (arrowed) between two consecutive particles (low-angle boundary)—Figure 13d.

The high magnification image in Figure 13e reveals the crystallographic orientation-relationship between the precipitates and the surrounding matrix, where the two particle/matrix interfaces seem to possess crystallographic orientations that differ from the matrix, indicating the commencement of incoherency and the formation of Θ -phase particles. Based on the inset in Figure 13e, the inter-planar distance is about 2.7 Å. The tendency

of transition of the precipitates from coherent to incoherency became more pronounced when the sample was tested at 240 °C, as shown in Figure 13f. Although the fast Fourier transition (FFT) pattern shown in the inset suggests strong coherency between the particle and the surrounding matrix, the observed deviation in the direction of the planes (⊙) indicates progressive incoherency.

Figure 14a is a bright field image produced from the B2N alloy (the sample was aged at 240 °C for 200 h), depicting the distribution of Al₂Cu particles formed by the remaining Cu in the matrix. As was shown in the SEM results presented in Section 3.2, a large amount of the Cu in the B2N alloy interacted with Ni, forming complex Al–Cu–Ni intermetallic particles, explaining the low volume fraction of the θ -Al₂Cu particles in Figure 14a compared to that observed in Figure 12a. The bright field image shown in Figure 14b depicts the distribution of Sc- and Zr-rich particles, whereas Figure 14d is a dark field image obtained from Figure 14c. The X-ray maps in Figures 14e and 14f show the distribution of Cu and Ni, respectively, in Figure 14c and highlighted by the tetragonal in Figure 14d. Figure 14g is a high-resolution electron image showing fusion/or nucleation of coherent particles (white circles) into/on an incoherent or semi-incoherent long particle, as depicted in the inset micrograph showing a difference between the direction of the planes of the particle and the surrounding matrix.

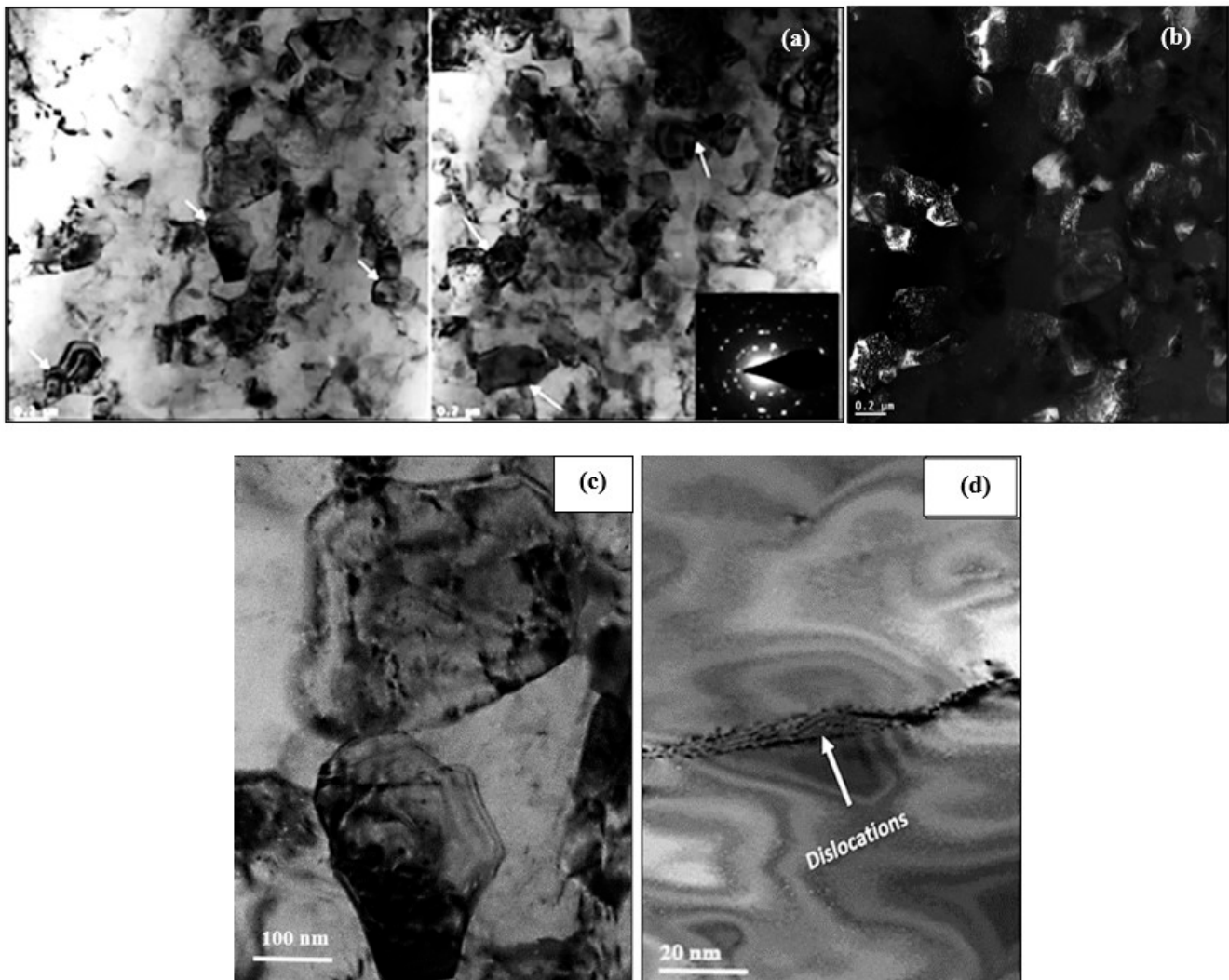


Figure 13. Cont.

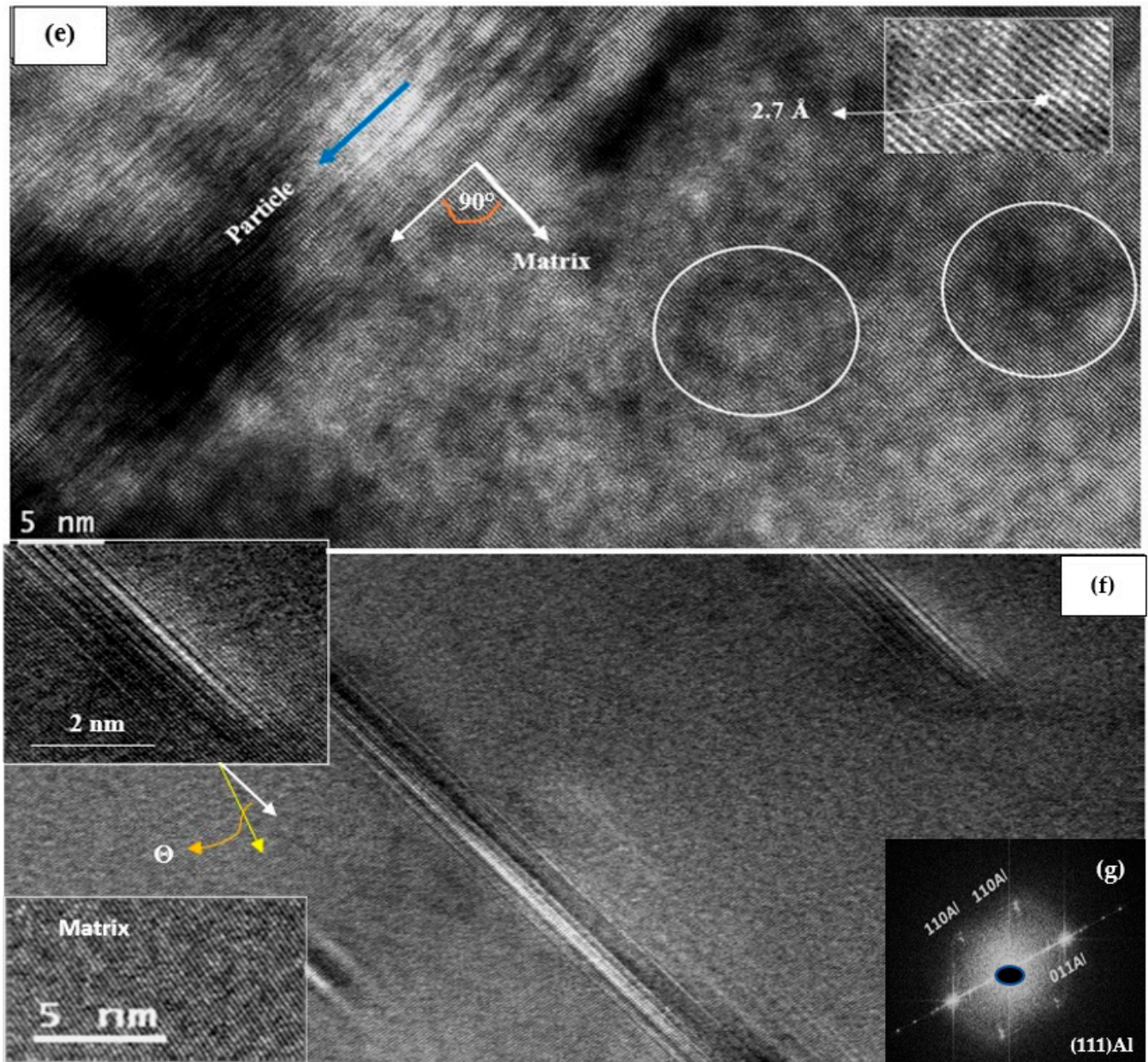


Figure 13. TEM images of the B alloy aged at 240 °C for 200 h: (a) composite bright field image, (b) corresponding dark field of (a); (c,d) bright field images showing an enlarged portion of two particles in (a); (e) high resolution electron image showing the transition from coherent particles (white circles) to incoherent ones (blue line); (f) high resolution electron image depicting the progressive increase in incoherent particles for samples tested at 240 °C—note all the three long precipitates are growing in the same direction; the white and yellow arrows-inset shows a gradual change in the interplanar orientation; (g) fast Fourier transition (FFT) pattern obtained for this image—extra points due to GPs/coherent precipitates.

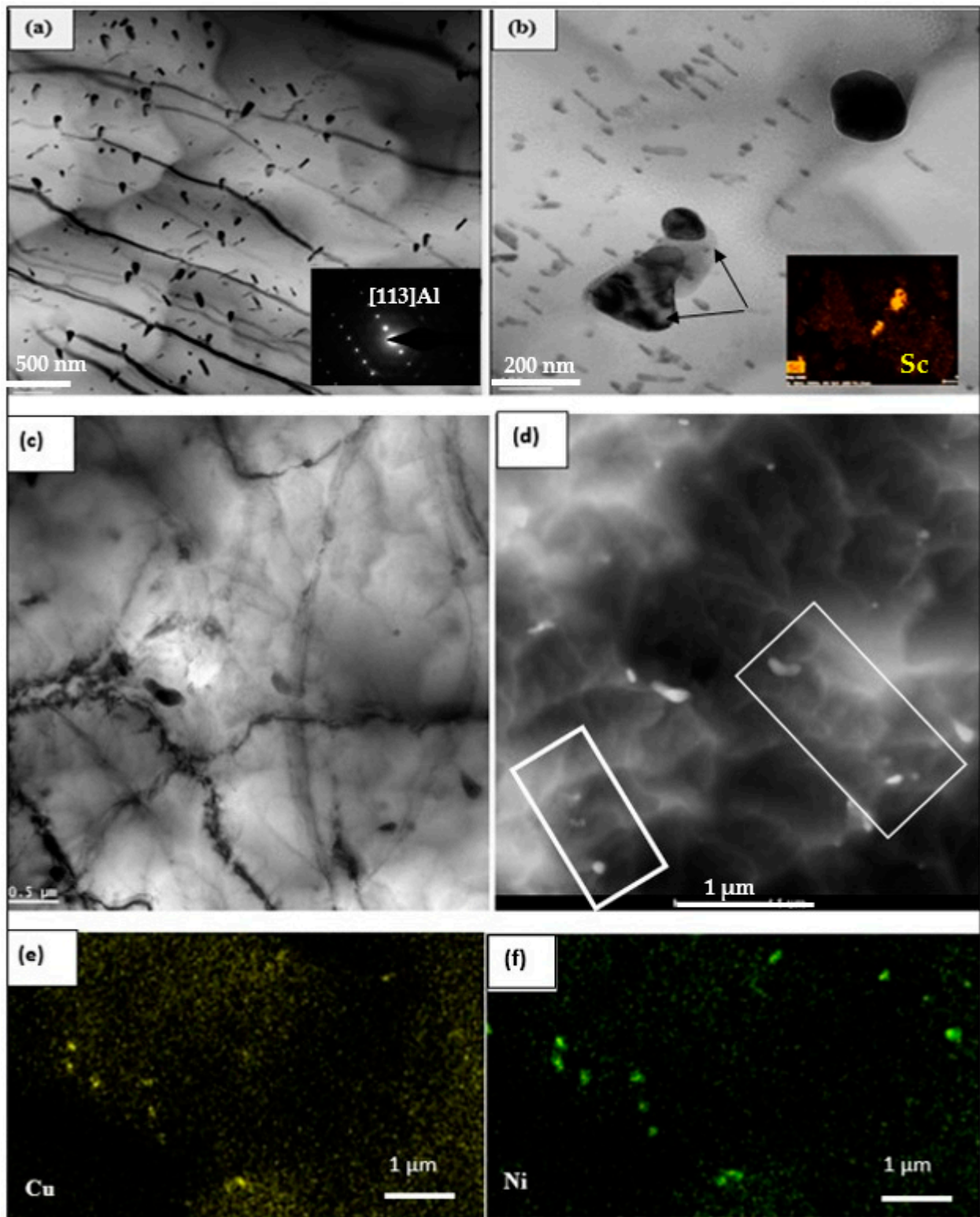


Figure 14. Cont.

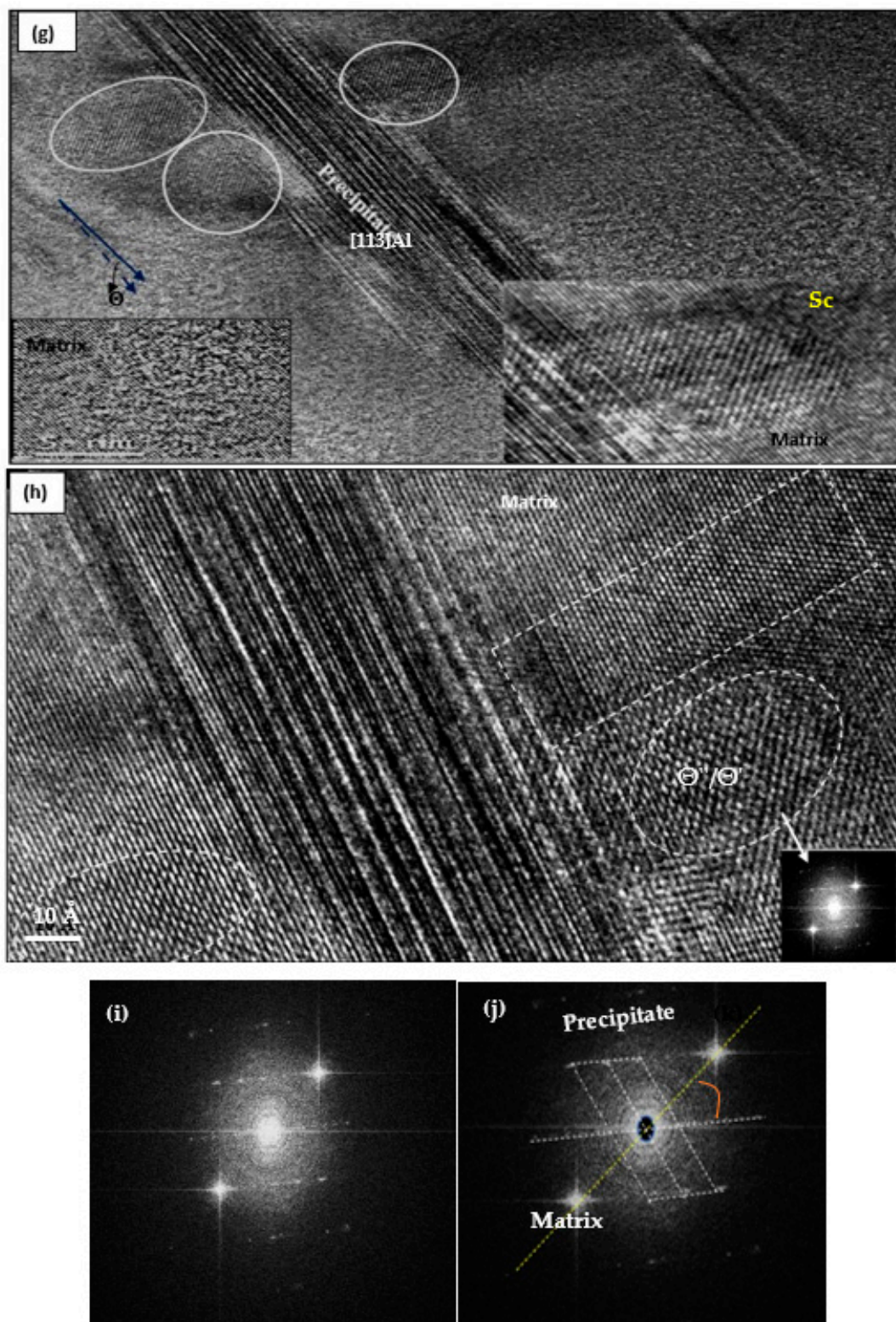


Figure 14. (a,b) TEM micrographs of the B2N alloy aged at 240 °C for 200 h bright field images—the black arrows in (b) point to Al_3Sc particles; (c) high magnification electron image of (a); (d) dark field image of (c) note the presence of very fine particles; (e,f) X-ray maps showing the distribution of Cu and Ni in (d) rectangular frames in (d) indicate the areas from which the Cu–Ni particles were imaged for the X-ray mapping; (g) high-resolution electron image corresponding to (a); (h) a high magnification image taken from another area of the sample, confirming observations noted in (g), (i,j) fast Fourier transition (FFT) pattern corresponding to area marked Θ''/Θ' in (h).

The small angle Θ between the solid and broken blue arrows indicates the *commencement* of incoherency of the large particle. The upper portion of Figure 14g was further enlarged, and is presented in Figure 14h, revealing fine GPII zones giving rise to streaking in the FFT (inset), in addition to most likely an early form of the Θ'' phase. In addition, the interplanar distance of the matrix is still around 2.7 Å. It should be mentioned here that Θ measured in Figure 14g is relatively smaller than that reported in Figure 13f due to delay in the onset of incoherency [85–87]. Figure 14i is the fast Fourier transition (FFT) pattern obtained for Θ''/Θ' image in Figure 14h. At this stage, the precipitate forms a more symmetrical pattern (faint spots-white lines) with an angle with the yellow line (aluminum matrix) due to their coherency with the matrix. The precipitate has more closely packed diffraction patterns than the matrix, indicating that the precipitate has some planes with larger interplanar spacings than those of the aluminum matrix (bright spots). Idrac et al. [88] investigated the precipitation in Al–Cu system. Electron diffraction performed on all the model alloys detected only three phases. These phases are the α -Al, Θ -Al₂Cu, and η_2 -AlCu phases. The diffraction pattern presented in Figure 14i is close to some extent to [112]- Θ Al₂Cu in refs. [86–88].

The bright field micrograph presented in Figure 15a reveals the presence of a coarse Al–Cu–Ni particle, where precipitate-free zones (PFZs) emerged near the intermetallic particle areas. These zones are normally caused by coarse particles on the grain boundaries, leading to the depletion of Cu atoms in these zones [22,87–92]. Figure 15b is the EDS spectrum associated with the point marked X in Figure 15a, showing peaks due to Al, Cu, and Ni elements. According to Hofmeister [93] and Liu et al. [91], the observed twins in Figure 16a and confirmed by their corresponding selected area electron diffraction (SAED) pattern depicted in Figure 16b are fivefold twinned nanoparticles termed multiply-twinned particles (MTP) with composition of tetrahedra (Dh) decahedron and (Ic) icosahedron and crystallographic ordination of {1 1 1}/[1 1 2] type. Figure 16c displays the general distribution of Si and Al where the Si particles are having wavy boundaries instead of sharp ones observed in non-modified alloys.

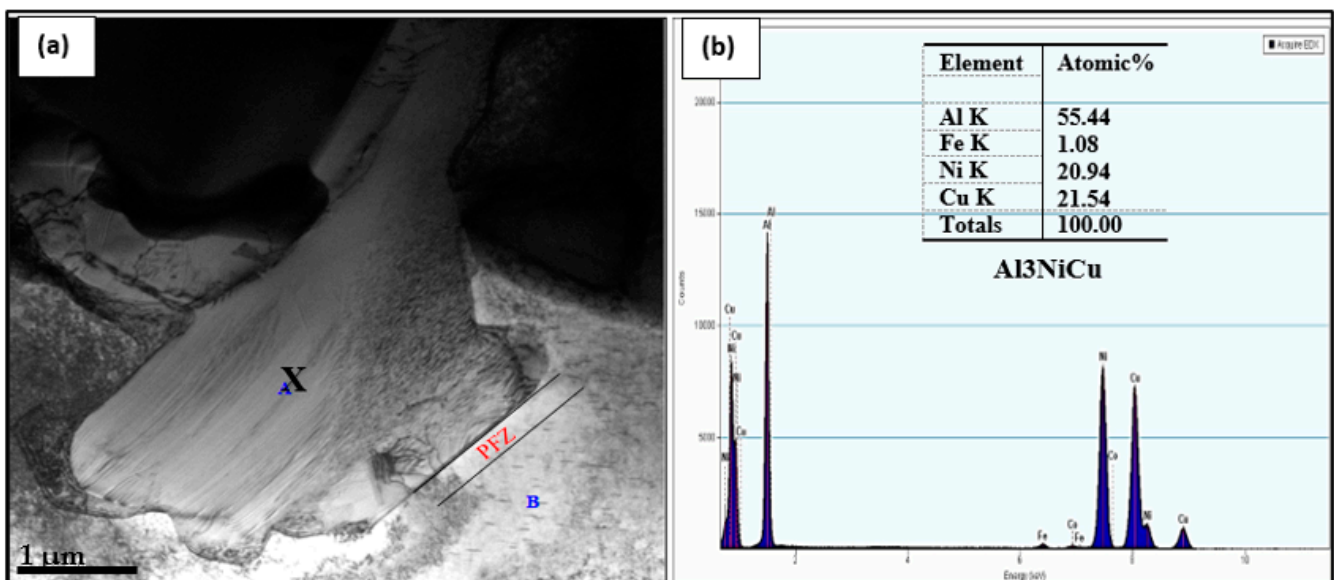


Figure 15. (a) Bright-field image of the B2N alloy sample aged for 200 h at 240 °C—revealing precipitation of a coarse Cu–Ni phase particle (marked A) in aluminum matrix (marked B), (b) EDS spectrum corresponding to the point marked X in (a) showing strong peaks due to Al, Cu, and Ni.

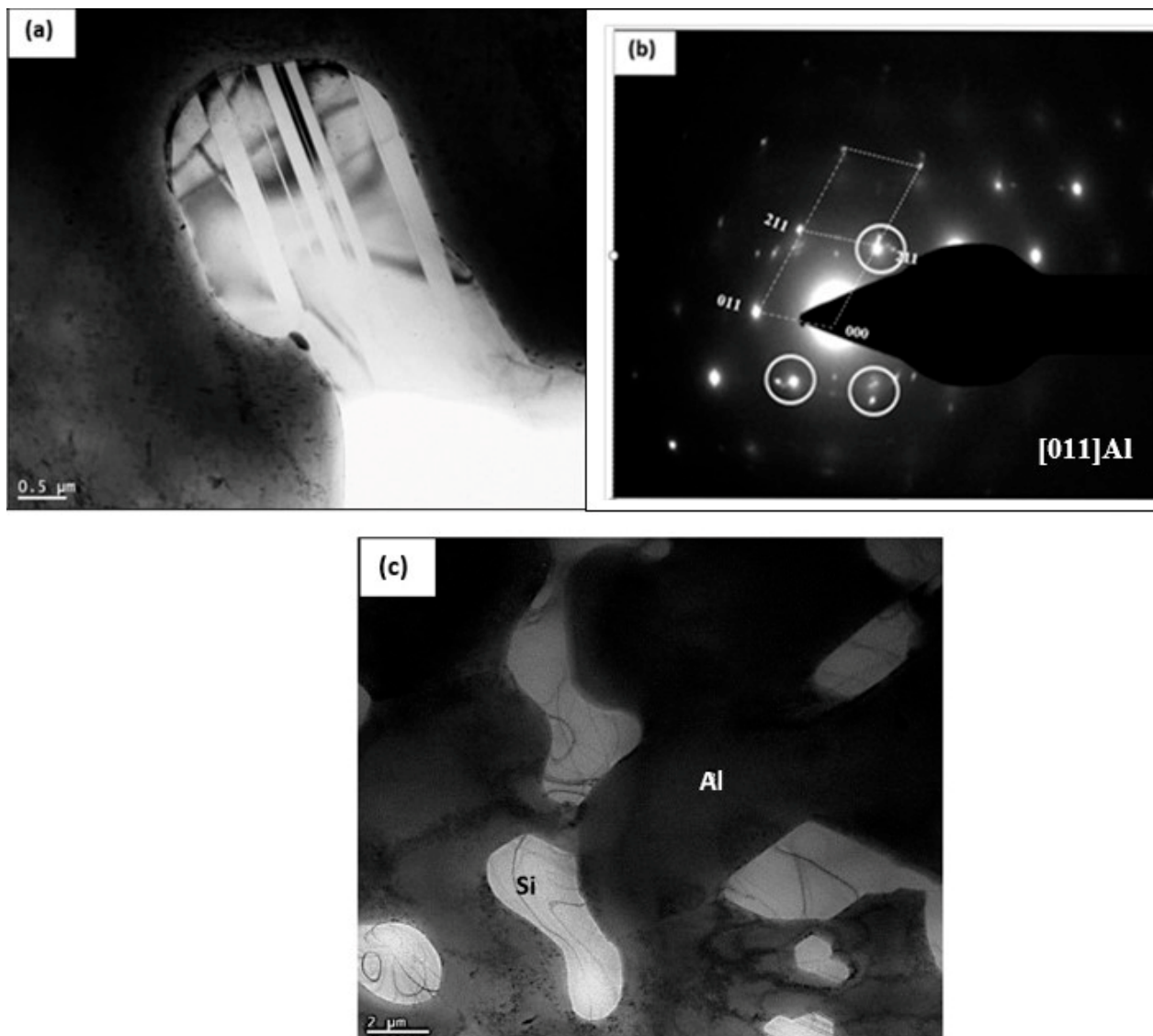


Figure 16. TEM micrograph of alloy the B2N alloy aged at 240 °C for 200 h: (a) bright field image-note the presence of twins within the Si particle, (b) selected area electron diffraction (SAED) pattern corresponding to (a) the white circles points to the presence of double zone axis caused by twinning, (c) general view of the Sr-modified eutectic Si particles.

4. Conclusions

Based on the findings presented in this study, the following conclusions may be drawn:

1. Aging of Al–Si–Cu–Mg alloys is characterized by the formation of multiple hardness peaks at the aging temperature with increasing aging time caused by simultaneous precipitation and coarsening of multiple phases.
2. Increasing the Ni content to 4 wt% improves the alloy resistance for softening during aging at 240 °C.
3. There are strong Cu–Ni, Zr–Ni, and Cu–Zr interactions between Cu, Ni, and Zr, causing a depletion in the matrix of Cu atoms needed for precipitation strengthening. This leads to a major reduction in the density of Al_2Cu phase particles, and hence a lowering of the alloy strength.
4. The Ni-rich compounds are observed to precipitate on the surface of precipitated primary Zr-phase particles.
5. Aging the base 354 alloy at 240 °C for a long period of 200 h enhances the coarsening of the precipitated Al_2Cu particles, leading to the commencement of incoherency.

6. In a 4 wt% Ni-containing alloy, a new phase was reported, namely $\text{Al}_3\text{Ni}_2\text{Cu}_2$, representing almost 50% (about 50 at%) of the compound composition.
7. Silicon particles were characterized by the presence of a large number of twins.
8. In the precipitation of primary Cu–Ni-rich particles, the particles are surrounded by precipitate-free zones due to depletion of Cu atoms in their vicinity.

Author Contributions: Methodology, E.S.; Validation, V.S.; Formal analysis, A.M.S.; Investigation, H.W.D.; Resources, SEM/TEM analysis F.H.S. All authors have read and agreed to the published version of the manuscript.

Funding: This research received no external funding.

Institutional Review Board Statement: Not applicable.

Informed Consent Statement: Not applicable.

Data Availability Statement: The original contributions presented in the study are included in the article. Further inquiries may be directed to the corresponding author.

Acknowledgments: The authors would like to thank Amal Samuel for enhancing the quality of the photos used in the present article. The authors would also like to extend thanks to David Liu, Facility for Electron Microscopy Research, McGill University for his consultation during the course of this research.

Conflicts of Interest: Author Herbert W. Doty was employed by the company General Motors Global Technology Center. The remaining authors declare that the research was conducted in the absence of any commercial or financial relationships that could be construed as a potential conflict of interest.

References

1. Wang, Y.; Fu, Y.; Yang, B.; Gao, M.; Guan, R. Deformation behavior and microstructure evolution induced by nano-sized Al6Mn phase particles in a homogenized Al–6Mg–0.8Mn alloy during hot compression. *Mater. Sci. Eng. A* **2023**, *882*, 145461. [[CrossRef](#)]
2. Yang, B.; Gao, M.; Liu, Y.; Pan, S.; Meng, S.; Fu, Y.; Guan, R. Formation mechanism of refined Al6 (Mn, Fe) phase particles during continuous rheo-extrusion and its contribution to tensile properties in Al–Mg–Mn–Fe alloys. *Mater. Sci. Eng. A* **2023**, *872*, 144952. [[CrossRef](#)]
3. Yang, B.; Wang, Y.; Gao, M.; Wang, C.; Guan, R. Microstructural evolution and strengthening mechanism of Al–Mg alloys with fine grains processed by accumulative continuous extrusion forming. *J. Mater. Sci. Technol.* **2022**, *128*, 195–204. [[CrossRef](#)]
4. Wang, Y.; Yang, B.; Gao, M.; Zhao, E.; Guan, R. Microstructure evolution, mechanical property response and strengthening mechanism induced by compositional effects in Al–6 Mg alloys. *Mater. Des.* **2022**, *220*, 111849. [[CrossRef](#)]
5. Moustafa, M. Effect of iron content on the formation of β -Al5FeSi and porosity in Al–Si eutectic alloys. *J. Mech. Work. Technol.* **2009**, *209*, 605–610. [[CrossRef](#)]
6. Yi, J.Z.; Gao, Y.X.; Lee, P.D.; Lindley, T.C. Effect of Fe-content on fatigue crack initiation and propagation in a cast aluminum–silicon alloy (A356–T6). *Mater. Sci. Eng.* **2004**, *386*, 396–407. [[CrossRef](#)]
7. Wu, X.; Zhang, H.; Ma, Z.; Tao, T.; Gui, J.; Song, W.; Yang, B.; Zhang, H. Interactions between Fe-rich intermetallics and Mg-Si phase in Al-7Si-xMg alloys. *J. Alloys Compd.* **2019**, *786*, 205–214. [[CrossRef](#)]
8. Timelli, G.; Caliarì, D.; Rakhmonov, J. Influence of Process Parameters and Sr Addition on the Microstructure and Casting Defects of LPDC A356 Alloy for Engine Blocks. *J. Mater. Sci. Technol.* **2016**, *32*, 515–523. [[CrossRef](#)]
9. Limodin, N.; Dahdah, N.; Wang, L.; El Bartali, A.; Witz, J.-F.; Buffiere, J.-Y.; Charkaluk, E. Characterisation of 3D strain heterogeneity at the microstructure scale during low cycle fatigue of an AlSi7Cu3Mg alloy at 250 °C. *Int. J. Fatigue* **2023**, *172*, 107476. [[CrossRef](#)]
10. Khisheh, S.; Azadi, M.; Hendoabadi, V.Z.; Parast, M.A.; Winter, G.; Seisenbacher, B.; Gruen, F.; Khalili, K. Influence of T6 heat-treating and over-ageing on out-of-phase thermo-mechanical fatigue behaviors of Al-Si-Cu alloy. *Mater. Today Commun.* **2022**, *33*, 104803. [[CrossRef](#)]
11. Siddiqui, R.; Abdul-Wahab, S.; Pervez, T. Effect of aging time and aging temperature on fatigue and fracture behavior of 6063 aluminum alloy under seawater influence. *Mater. Des.* **2008**, *29*, 70–79. [[CrossRef](#)]
12. Sadeler, R.; Totik, Y.; Gavgalı, M.; Kaymaz, I. Improvements of fatigue behaviour in 2014 Al alloy by solution heat treating and age-hardening. *Mater. Des.* **2004**, *25*, 439–445. [[CrossRef](#)]
13. Wang, G.; Bian, X.; Wang, W.; Zhang, J. Influence of Cu and minor elements on solution treatment of Al–Si–Cu–Mg cast alloys. *Mater. Lett.* **2003**, *57*, 4083–4087. [[CrossRef](#)]
14. Chen, B.A.; Pan, L.; Wang, R.H.; Liu, G.; Cheng, P.M.; Xiao, L.; Sun, J. Effect of solution treatment on precipitation behaviors and age hardening response of Al–Cu alloys with Sc addition. *Mater. Sci. Eng. A* **2011**, *530*, 607–617. [[CrossRef](#)]

15. Tavitans-Medrano, F.; Gruzleski, J.; Samuel, F.; Valtierra, S.; Doty, H. Effect of Mg and Sr-modification on the mechanical properties of 319-type aluminum cast alloys subjected to artificial aging. *Mater. Sci. Eng. A* **2007**, *480*, 356–364. [[CrossRef](#)]
16. Abdelaziz, M.H.; Elgallad, E.M.; Doty, H.W.; Samuel, F.H. Strengthening precipitates and mechanical performance of Al–Si–Cu–Mg cast alloys containing transition elements. *Mater. Sci. Eng. A* **2021**, *820*, 141497. [[CrossRef](#)]
17. De Wilde, J.; Froyen, L.; Rex, S. Coupled two-phase [$\alpha(\text{Al}) + \theta(\text{Al}_2\text{Cu})$] planar growth and destabilisation along the univariant eutectic reaction in Al–Cu–Ag alloys. *Scr. Mater.* **2004**, *51*, 533–538. [[CrossRef](#)]
18. Weng, Y.; Chen, J.; Cheng, X.; Ding, L.; Sun, Q.; Tao, S.; Liu, X.; Jia, Z. Interface structures and thickening mechanisms of the Q' and QP2 phases for Al–Mg–Si–Cu alloys. *Mater. Charact.* **2022**, *194*, 11235. [[CrossRef](#)]
19. Ding, L.; Jia, Z.; Nie, J.-F.; Weng, Y.; Cao, L.; Chen, H.; Wu, X.; Liu, Q. The structural and compositional evolution of precipitates in Al–Mg–Si–Cu alloy. *Acta Mater.* **2018**, *145*, 437–450. [[CrossRef](#)]
20. Li, Z.; Samuel, A.M.; Samuel, F.H.; Ravindran, C.; Valtierra, S. Effect of alloying elements on the segregation and dissolution of CuAl₂ phase in Al–Si–Cu 319 alloys. *J. Mater. Sci.* **2003**, *38*, 1203–1218. [[CrossRef](#)]
21. Meyers, C.; Hinton, K.; Chou, J.-S. Towards the Optimization of Heat-Treatment in Aluminium Alloys. *Mater. Sci. Forum* **1992**, *102*, 75–84. [[CrossRef](#)]
22. Mohamed, A.M.A.; Samuel, F.H. A review on the heat treatment of Al–Si–Cu/Mg casting alloys. In *Heat Treatment-Conventional and Novel Applications*; In Tech: London, UK, 2012; p. 229.
23. Apelian, D. *Aluminum Cast Alloys: Enabling Tools for Improved Performance*; North American Die Casting Association: New York, NY, USA, 2009.
24. Wang, Q. Microstructural Effects on the Tensile and Fracture Behavior of Aluminum Casting Alloys A356/357. *Metall. Mater. Trans. A* **2003**, *34*, 2887–2899. [[CrossRef](#)]
25. Nakashima, K.; Miyamoto, K.; Kunimine, T.; Monzen, R.; Muramatsu, N. Precipitation behavior of Cu–Zr compounds in a Cu–0.13 wt%Zr alloy. *J. Alloys Compd.* **2020**, *816*, 152650. [[CrossRef](#)]
26. Fadayomi, O.; Sanders, P.G.; Odegard, G.M. Microstructure and properties of precipitation-hardened Zr and Zn–Zr based aluminum alloys. *J. Alloys Compd.* **2019**, *788*, 1218–1230. [[CrossRef](#)]
27. Nakamura, J.; Matsuda, K.; Sato, T.; Marioara, C.D.; Andersen, S.J.; Holmestad, R.; Ikeno, S. The Crystal Structure of the β' -Phase Including Ag in Al–Mg–Si–Ag Alloy. *Adv. Mater. Res. Trans. Tech. Publ.* **2012**, *409*, 67–70. [[CrossRef](#)]
28. Medrano-Prieto, H.M.; Garay-Reyes, C.G.; Gómez-Esparza, C.D.; Aguilar-Santillán, J.; Maldonado-Orozco, M.C.; Martínez-Sánchez, R. Evolution of Microstructure in Al–Si–Cu System Modified with a Transition Element Addition and its Effect on Hardness. *Mater. Res.* **2016**, *19*, 59–66. [[CrossRef](#)]
29. Hamasha, M.M.; Mayyas, A.T.; Hassan, A.M.; Hayajneh, M.T. The effect of time, percent of copper and nickel on naturally aged Al–Cu–Ni cast alloys. *J. Miner. Mater. Charact. Eng.* **2012**, *11*, 117–131. [[CrossRef](#)]
30. Bogdanoff, T.; Dahle, A.K.; Seifeddine, S. Effect of Co and Ni Addition on the Microstructure and Mechanical Properties at Room and Elevated Temperature of an Al–7%Si Alloy. *Int. J. Met.* **2017**, *12*, 434–440. [[CrossRef](#)]
31. Abdelaziz, M.H.; Samuel, A.M.; Doty, H.W.; Valtierra, S.; Samuel, F.H. Effect of additives on the microstructure and tensile properties of Al–Si alloys. *J. Mater. Res. Technol.* **2019**, *8*, 2255–2268. [[CrossRef](#)]
32. Medrano-Prieto, H.; Garay-Reyes, C.; Estrada-Guel, I.; Mendoza-Duarte, J.; Guía-Tello, J.; Ochoa-Gamboa, R.; Ornelas-Gutiérrez, C.; Rodríguez-Cabriales, G.; Castro-Carmona, J.; Camacho-Montes, H.; et al. Effect of Ni additions and hot deformation on precipitation behavior and hardness in Al–Si–Mg aged alloys. *J. Alloys Compd.* **2020**, *828*, 154429. [[CrossRef](#)]
33. Zuo, L.; Ye, B.; Feng, J.; Xu, X.; Kong, X.; Jiang, H. Effect of δ -Al₃CuNi phase and thermal exposure on microstructure and mechanical properties of Al–Si–Cu–Ni alloys. *J. Alloys Compd.* **2019**, *791*, 1015–1024. [[CrossRef](#)]
34. Cai, Q.; Fang, C.; Mendis, C.; Chang, I.T.; Cantor, B. Thermal behaviour and microstructure evolution of new ternary eutectic alloy in Al–Cu–Si–Ni system. *J. Alloys Compd.* **2023**, *941*, 168942. [[CrossRef](#)]
35. Czerwinski, F.; Aniolek, M.; Li, J. Strengthening retention and structural stability of the Al–Al₃Ni eutectic at high temperatures. *Scr. Mater.* **2022**, *214*, 114679. [[CrossRef](#)]
36. Bayram, Ü.; Maraşlı, N. Influence of Growth Rate on Eutectic Spacing, Microhardness, and Ultimate Tensile Strength in the Directionally Solidified Al–Cu–Ni Eutectic Alloy. *Met. Mater. Trans. B* **2018**, *49*, 3293–3305. [[CrossRef](#)]
37. Li, G.J.; Guo, M.X.; Wang, Y.; Zheng, C.H.; Zhang, J.S.; Zhuang, L.Z. Effect of Ni addition on microstructure and mechanical properties of Al–Mg–Si–Cu–Zn alloys with a high Mg/Si ratio. *Int. J. Min. Met. Mater.* **2019**, *26*, 740–751. [[CrossRef](#)]
38. Abdelaziz, M.; Doty, H.; Valtierra, S.; Samuel, F. Static versus dynamic thermal exposure of transition elements-containing Al–Si–Cu–Mg cast alloy. *Mater. Sci. Eng. A* **2018**, *739*, 499–512. [[CrossRef](#)]
39. Darlapudi, A.; McDonald, S.D.; StJohn, D.H. The influence of Cu, Mg and Ni on the solidification and microstructure of Al–Si alloys. *IOP Conf. Ser. Mater. Sci. Eng.* **2016**, *117*, 012022. [[CrossRef](#)]
40. Milligan, B.; Ma, D.; Allard, L.; Clarke, A.; Shyam, A. Dislocation- θ' (Al₂Cu) interactions during creep deformation of an Al–Cu alloy. *Scr. Mater.* **2022**, *217*, 114739. [[CrossRef](#)]
41. Belov, N.A.; Eskin, D.G.; Avxentieva, N.N. Constituent phase diagrams of the Al–Cu–Fe–Mg–Ni–Si system and their application to the analysis of aluminium piston alloys. *Acta Mater.* **2005**, *53*, 4709–4722. [[CrossRef](#)]
42. Hernandez-Sandoval, J.; Zedan, Y.; Garza-Elizondo, G.H.; Abdelaziz, M.H.; Songmene, V.; Samuel, F.H. Effect of Minor Addition of Ni and Zr on the High-Temperature Performance of Al–Si–Cu–Mg Cast Alloys. *Int. J. Met.* **2022**, *16*, 1235–1251. [[CrossRef](#)]

43. Djurdjevic, M.B.; Manasijevic, S. Impact of major alloying elements on the solidification parameters of cast hypoeutectic AlSi6Cu (1–4 wt.%) and AlSi8Cu (1–4 wt.%) alloys. *Metall. Mater. Eng.* **2014**, *20*, 235–246. [[CrossRef](#)]
44. Hernandez-Sandoval, J.; Garza-Elizondo, G.H.; Abdelaziz, M.H.; Samuel, A.M.; Doty, H.W.; Samuel, F.H. The Effect of Ni and Zr Additions on the Tensile Properties of Isothermally Aged Al–Si–Cu–Mg Cast Alloys. *Int. J. Met.* **2021**, *16*, 435–457. [[CrossRef](#)]
45. Medrano-Prieto, H.; Garay-Reyes, C.; Gómez-Esparza, C.; Estrada-Guel, I.; Aguilar-Santillan, J.; Maldonado-Orozco, M.; Martínez-Sánchez, R. Effect of Nickel addition and solution treatment time on microstructure and hardness of Al–Si–Cu aged alloys. *Mater. Charact.* **2016**, *120*, 168–174. [[CrossRef](#)]
46. Hernandez-Sandoval, J.; Samuel, A.M.; Valtierra, S.; Samuel, F.H. Ni- and Zr-Based Intermetallics in Al–Si–Cu–Mg Cast Alloys. *Metallogr. Microstruct. Anal.* **2014**, *3*, 408–420. [[CrossRef](#)]
47. Chen, Y.; Zhang, Z.; Chen, Z.; Tsalanidis, A.; Weyland, M.; Findlay, S.; Allen, L.J.; Li, J.; Medhekar, N.V.; Bourgeois, L. The enhanced theta-prime (θ') precipitation in an Al–Cu alloy with trace Au additions. *Acta Mater.* **2017**, *125*, 340–350. [[CrossRef](#)]
48. Abdelaziz, M.H.; Samuel, A.M.; Doty, H.W.; Songmene, V.; Samuel, F.H. Mechanical Performance and Precipitation Behavior in Al–Si–Cu–Mg Cast Alloys: Effect of Prolonged Thermal Exposure. *Materials* **2022**, *15*, 2830. [[CrossRef](#)]
49. Zhou, L.; Wu, C.L.; Xie, P.; Niu, F.J.; Ming, W.Q.; Du, K.; Chen, J.H. A hidden precipitation scenario of the θ' -phase in Al–Cu alloys. *J. Mater. Sci. Technol.* **2021**, *75*, 126–138. [[CrossRef](#)]
50. Mohamed, A.M.A.; Ibrahim, M.F.; Samuel, E.; Samuel, A.M.; Samuel, F.H.; Doty, H.W. Assessment of the Effect of Mg Addition on the Solidification Behavior, Tensile and Impact Properties of Al–Si–Cu Cast Alloys. *Int. J. Met.* **2022**, *17*, 82–108. [[CrossRef](#)]
51. Joenoes, A.; Gruzleski, J. Magnesium effects on the microstructure of unmodified and modified Al–Si alloys. *Cast Metals* **1991**, *4*, 62–71. [[CrossRef](#)]
52. Drouzy, M.; Jacob, S.; Richard, M. Interpretation of 749 tensile results by means of quality index and probable yield strength-application to Al–Si7 Mg foundry alloys-France. *Int. Cast Met. J.* **1980**, *5*, 43–50.
53. Jacob, S. Quality index in prediction of properties of 755 aluminum castings—A review. In Proceedings of the Transactions of the American Foundry Society and the One Hundred Fourth Annual Castings Congress, Pittsburgh, PA, USA, 8–11 April 2000; pp. 709–712.
54. Shaha, S.K. Development and Characterization of Cast Modified Al–Si–Cu–Mg Alloys for Heat Resistant Power Train Applications. Ph.D. Thesis, Ryerson University, Toronto, ON, Canada, 2015.
55. Sankanit, P.; Uthaisangasuk, V.; Pandee, P. Tensile properties of hypoeutectic Al–Ni alloys: Experiments and FE simulations. *J. Alloys Compd.* **2021**, *889*, 161664. [[CrossRef](#)]
56. Engin, S.; Büyük, U.; Maraşlı, N. The effects of microstructure and growth rate on microhardness, tensile strength, and electrical resistivity for directionally solidified Al–Ni–Fe alloys. *J. Alloys Compd.* **2016**, *660*, 23–31. [[CrossRef](#)]
57. Bäckerud, L.; Chai, G.; Tamminen, J. *Solidification Characteristics of Aluminium Alloys, Volume 2: Foundry Alloys*; AFS/Skanaluminium: Des Plaines, IL, USA, 1990; pp. 71–84.
58. Wang, J.; Reif, W. Effect of Cu Content on Grain Refinement of an Al–Cu Alloy AlTiSbI Refiners. *Int. J. Mater. Res.* **1993**, *84*, 445–450. [[CrossRef](#)]
59. Medrano-Prieto, H.M.; Garay-Reyes, C.; Gómez-Esparza, C.; Martínez-Sánchez, R. Influence of Solute Addition in the Microstructure and Hardness of the Al–Si–Cu Alloys. *MRS Proc.* **2016**, *1815*, 92. [[CrossRef](#)]
60. Chen, Z.; Kang, H.; Fan, G.; Li, J.; Lu, Y.; Jie, J.; Zhang, Y.; Li, T.; Jian, X.; Wang, T. Grain refinement of hypoeutectic Al–Si alloys with B. *Acta Mater.* **2016**, *120*, 168–178. [[CrossRef](#)]
61. Nadendla, H.B.; Nowak, M.; Bolzoni, L. Grain Refiner for Al–Si Alloys. In *Light Metals 2013*; Sadler, B.A., Ed.; The Minerals, Metals & Materials Series; Springer International Publishers: New York, NY, USA, 2016. [[CrossRef](#)]
62. Wang, T.; Fu, H.; Chen, Z.; Xu, J.; Zhu, J.; Cao, F.; Li, T. A novel fading-resistant Al–3Ti–3B grain refiner for Al–Si alloys. *J. Alloys Compd.* **2012**, *51*, 45–49. [[CrossRef](#)]
63. Shaha, S.K.; Czerwinski, F.; Kasprzak, W.; Friedman, J.; Chen, D.L. Effect of Zr, V and Ti on hot compression behavior of the Al–Si cast alloy for powertrain applications. *J. Alloys Compd.* **2014**, *615*, 1119–1131. [[CrossRef](#)]
64. Abdelaziz, M.H.; Elsharkawi, E.A.; Doty, H.W.; Samuel, F.H. Mechanical Performance of Zr-Containing 354-Type Al–Si–Cu–Mg Cast Alloy: Role of Geometrical Discontinuities. *J. Mater. Eng. Perform.* **2020**, *29*, 6640–6651. [[CrossRef](#)]
65. Rakhmonov, J.; Timelli, G.; Bonollo, F. Characterization of the solidification path and microstructure of secondary Al–7Si–3Cu–0.3Mg alloy with Zr, V and Ni additions. *Mater. Charact.* **2017**, *128*, 100–108. [[CrossRef](#)]
66. Garza-Elizondo, G.H.; Elsharkawi, E.A.; Samuel, A.M.; Doty, H.W.; Samuel, F.H. Effects of Alloying Elements Additions on Ambient Temperature Performance of Al–Si–Cu–Mg Base Alloys. *Int. J. Met.* **2021**, *15*, 1385–1401. [[CrossRef](#)]
67. Biswas, A.; Siegel, D.J.; Seidman, D.N. Compositional evolution of Q-phase precipitates in an aluminum alloy. *Acta Mater.* **2014**, *75*, 322–336. [[CrossRef](#)]
68. Bobel, A.; Kim, K.; Wolverton, C.; Walker, M.; Olson, G.B. Equilibrium composition variation of Q-phase precipitates in aluminum alloys. *Acta Mater.* **2017**, *138*, 150–160. [[CrossRef](#)]
69. Pan, X.; Morral, J.E.; Brody, H.D. Predicting the Q-Phase in Al–Cu–Mg–Si Alloys. *J. Phase Equilib. Diffus.* **2010**, *31*, 144–148. [[CrossRef](#)]
70. Qian, H.; Zhu, D.; Hu, C.; Jiang, X. Effects of Zr Additive on Microstructure, Mechanical Properties, and Fractography of Al–Si Alloy. *Metals* **2018**, *8*, 124. [[CrossRef](#)]

71. Gao, T.; Ceguerra, A.; Breen, A. Precipitation behaviors of cubic and tetragonal Zr-rich phase in Al–(Si–) Zr alloys. *J. Alloys Compd.* **2016**, *674*, 125–130. [[CrossRef](#)]
72. Rakhmonov, J.; Timelli, G.; Bonollo, F. The Effect of Transition Elements on High-Temperature Mechanical Properties of Al–Si Foundry Alloys—A Review. *Adv. Eng. Mater.* **2016**, *18*, 1187–1298. [[CrossRef](#)]
73. Wang, N.; Li, C.; Du, Z.; Wang, F. Experimental study and thermodynamic re-assessment of the Ni–Zr system. *Calphad* **2007**, *31*, 413–421. [[CrossRef](#)]
74. Delogu, F.; Cocco, G. Numerical simulations of structural modifications at a Ni–Zr sliding interface. *Phys. Rev. B* **2005**, *72*, 014124. [[CrossRef](#)]
75. Kulikova, T.V.; Majorova, A.V.; Yu, K.; Shunyaev, K.Y.; Ryltsev, R.E. Thermodynamic properties of Cu–Zr melts: The role of chemical interaction. *Phys. B Condens. Matter* **2015**, *466–467*, 90–95. [[CrossRef](#)]
76. Kim, Y.M.; Lee, B.J. A modified embedded-atom method interatomic potential for the Cu–Zr system. *J. Mater. Res.* **2008**, *23*, 1095–1104. [[CrossRef](#)]
77. Dorin, T.; Ramajayam, M.; Justin Lamb, J.; Langan, T. Effect of Sc and Zr additions on the microstructure/strength of Al–Cu binary alloys. *Mater. Sci. Eng. A* **2017**, *707*, 58–64. [[CrossRef](#)]
78. Król, J. The precipitation strengthening of directionally solidified Al Si Cu alloys. *Mater. Sci. Eng. A* **1997**, *234–236*, 169–172. [[CrossRef](#)]
79. Weakley-Bollin, S.C.; Donlon, W.; Donlon, W.; Wolverton, C.; Allison, J.E.; Jones, J.W. Modeling the age-hardening behavior of Al–Si–Cu alloys. *Met. Mater Trans A* **2004**, *35*, 2407–2418. [[CrossRef](#)]
80. Dong, X.; Guo, Y.; Wang, J.; Xia, F.; Ma, K.; Duan, H.; Yang, Z.; Wang, P.; Liang, M.; Li, J. Novel AlCu solute cluster precipitates in the Al–Cu alloy by elevated aging and the effect on the tensile properties. *Mater. Sci. Eng. A* **2023**, *862*, 144454. [[CrossRef](#)]
81. Casas, B.Y.; Figueroa, I.A.; González, G.; González-Ojeda, R.; Alfonso, I. Dissolution of the second phases and transformation from Mg₂Si to Q–Al₅Cu₂Mg₈Si₆ in solution heat treated quaternary Al-alloys. *J. Alloys Compd.* **2023**, *955*, 170003. [[CrossRef](#)]
82. Piao, Y.; Jia, H.; Zha, M.; Ma, P.-K.; Gao, D.; Yin, C.-R.; Yang, Z.-Z.; Wang, H.-Y. The effect of quenching rates on microstructure and mechanical properties of an Al–Si–Cu–Mg alloy. *Mater. Charact.* **2023**, *196*, 112609. [[CrossRef](#)]
83. Ibrahim, M.F.; Samuel, A.M.; Doty, H.W.; Samuel, H. Effect of Aging Conditions on Precipitation Hardening in Al–Si–Mg and Al–Si–Cu–Mg Alloys. *Inter Met.* **2017**, *11*, 274–286. [[CrossRef](#)]
84. Xiao, Q.; Liu, H.; Yi, D.; Yin, D.; Chen, Y.; Zhang, Y.; Wang, B. Effect of Cu content on precipitation and age-hardening behavior in Al–Mg–Si–xCu alloys. *J. Alloys Compd.* **2017**, *695*, 1105–1113. [[CrossRef](#)]
85. Starke, E. *Accelerated Aging of Materials and Structures: The Effects of Long-Term Elevated-Temperature Exposure*; NMAB-479; National Materials Advisory Board, National Research Council: Washington, DC, USA, 1996.
86. Weatherly, G.; Nicholson, R. An Electron Microscope Investigation of the Interfacial Structure of Semi-Coherent Precipitates. *Philos. Mag.* **1968**, *17*, 801–831. [[CrossRef](#)]
87. Buha, J.; Lumley, R.N.; Crosky, A.G. Secondary ageing in an aluminium alloy 7050. *Mater. Sci. Eng. A* **2008**, *492*, 1–11. [[CrossRef](#)]
88. Idrac, J.; Blanc, C.; Kihn, Y.; Lafont, M.C.; Mankowski, G.; Skeldon, P.; Thompson, G.E. Electrochemical Behavior of Magnetron-Sputtered Al–Cu Alloy Films in Sulfate Solutions. *J. Electrochem. Soc.* **2007**, *154*, C286. [[CrossRef](#)]
89. Tolley, A.; Mitlin, D.; Radmilovic, V.; Dahmen, U. Transmission electron microscopy analysis of grain boundary precipitate-free-zones (PFZs) in an AlCuSiGe alloy. *Mater. Sci. Eng. A* **2005**, *412*, 204–213. [[CrossRef](#)]
90. Showe, P.; Poplawsky, J.; Bahl, S.; Shyam, A. The role of Si in determining the stability of the θ' precipitate in Al–Cu–Mn–Zr alloys. *J. Alloys Compd.* **2021**, *862*, 158152. [[CrossRef](#)]
91. Liu, H.; Papadimitriou, I.; Lin, F.X.; LLorca, J. Precipitation during high temperature aging of Al–Cu alloys: A multiscale analysis based on first principles calculations. *Acta Mater.* **2019**, *167*, 121–135. [[CrossRef](#)]
92. Hu, Y.; Wang, G.; Ji, Y. Study of θ' precipitation behavior in Al–Cu–Cd alloys by phase-field modeling. *Mater. Sci. Eng. A* **2019**, *746*, 105–114. [[CrossRef](#)]
93. Hofmeister, H. Fivefold Twinned Nanoparticles. *Encycl. Nanosci. Nanotechnol.* **2004**, *3*, 431–452.

Disclaimer/Publisher’s Note: The statements, opinions and data contained in all publications are solely those of the individual author(s) and contributor(s) and not of MDPI and/or the editor(s). MDPI and/or the editor(s) disclaim responsibility for any injury to people or property resulting from any ideas, methods, instructions or products referred to in the content.